Evaluating the Response of Diurnal Variations in Surface and Air Temperature to Evaporative Conditions across Vegetation Types in FLUXNET and ERA5

ANNU PANWAR[a] AND AXEL KLEIDON[a]

[a] Max Planck Institute for Biogeochemistry, Jena, Germany

ABSTRACT: The diurnal variations of surface and air temperature are closely related, but their different responses to evaporative conditions can inform us about land–atmosphere interactions. Here, we evaluate the responses of the diurnal ranges in surface (ΔT_s) and air (ΔT_a) temperature to evaporative fraction at 160 FLUXNET sites and in the ERA5 reanalysis. We show that the sensitivity of ΔT_s to evaporative fraction depends on vegetation type, whereas ΔT_a does not. On days with low evaporative fraction, ΔT_s in FLUXNET is enhanced by up to ~20 K (~30 K in ERA5) in short vegetation, but only by up to ~10 K (~10 K in ERA5) in forests. Note that ΔT_a responds rather similarly to evaporative fraction irrespective of vegetation type (~5 K in FLUXNET, ~10 K in ERA5). We find a systematic bias in ERA5's ΔT response to evaporative conditions, showing a stronger sensitivity to evaporative fraction than in FLUXNET. We then demonstrate with a simple atmospheric boundary layer (SABL) model that the weak response of ΔT_a to evaporative fraction can be explained by greater boundary layer growth under dry conditions, which increases the heat storage capacity and reduces the response of air temperature to evaporative fraction. Additionally, using a simplified surface energy balance (SSEB) model we show that ΔT_s mainly responds to solar radiation, evaporative fraction, and aerodynamic conductance. We conclude that the dominant patterns of diurnal temperature variations can be explained by fundamental physical concepts, which should help us to better understand the main controls of land–atmosphere interactions.

SIGNIFICANCE STATEMENT: Generally, air temperature is used more widely than the surface temperature, and often they are assumed to be equivalent. However, we show that their responses to changes in vegetation type and evaporative conditions are quite different. Using FLUXNET observations, ERA5 reanalysis, and two simple physical models, we found that these responses are much stronger in surface temperature, especially in short vegetation, and relatively weaker in air temperature. Despite being measured just 2 m above the surface, air temperature carries lesser imprints of evaporation and vegetation than the surface temperature because of boundary layer dynamics. These findings suggest the importance of coupled land–atmosphere processes in shaping surface and air temperature differently and provide insights on their distinctive responses to global changes.

KEYWORDS: Boundary layer; Vegetation; Atmosphere-land interaction; Evaporation; Surface temperature; Energy budget/balance

---

1. Introduction

The diurnal temperature range (DTR) is a vital index for describing how atmospheric conditions over land change during the day and is used as an indicator of global change (Karl et al. 1991; Easterling et al. 1997; Braganza et al. 2004; Lewis and Karoly 2013). Therefore, understanding the physical processes that shape DTR is crucial. Previous studies have shown that soil moisture, solar radiation, and vegetation types are among the leading controlling factors of DTR (Dai et al. 1997, 1999; Stone and Weaver 2002; Feddema et al. 2005; Zhou et al. 2009; Pyrgou et al. 2019). For instance, Mearns et al. (1995) showed that 52% of variance in DTR can be explained by evaporative cooling, while Makowski et al. (2009) demonstrate a strong correlation ($R^2 \approx 0.87$) between the annual mean of DTR and solar radiation. Recently, greater attention is given to quantify the consequences of deforestation and land use/land cover change on DTR (Gallo et al. 1996; Collatz et al. 2000; Zhou et al. 2007). For instance, Lobell and Bonfils (2008) estimated a mean decrease of DTR by 5°C due to irrigation in California.

Typically, in these studies, the diurnal range of air temperature (DTR of air temperature, hereafter ΔT_a) is used due to the widespread availability of air temperature products, which are measured at ~2-m height above the ground at meteorological stations. However, advances in remote sensing and land surface modeling have encouraged the use of surface temperature, the radiative temperature of the surface or canopy, also known as skin temperature, which can be obtained using the Stefan–Boltzmann law. These products have stimulated discussions on the different responses of ΔT_a and the diurnal range of surface temperature (DTR of surface temperature, hereafter ΔT_s) to changes in water availability and vegetation characteristics (Zhou et al. 2007; Jin and Dickinson 2010; Baldocchi and Ma 2013). In this study, we investigate the extent to which ΔT_s and ΔT_a respond differently to evaporative conditions, vegetation properties, and the physical constraints governing these responses across different climates.

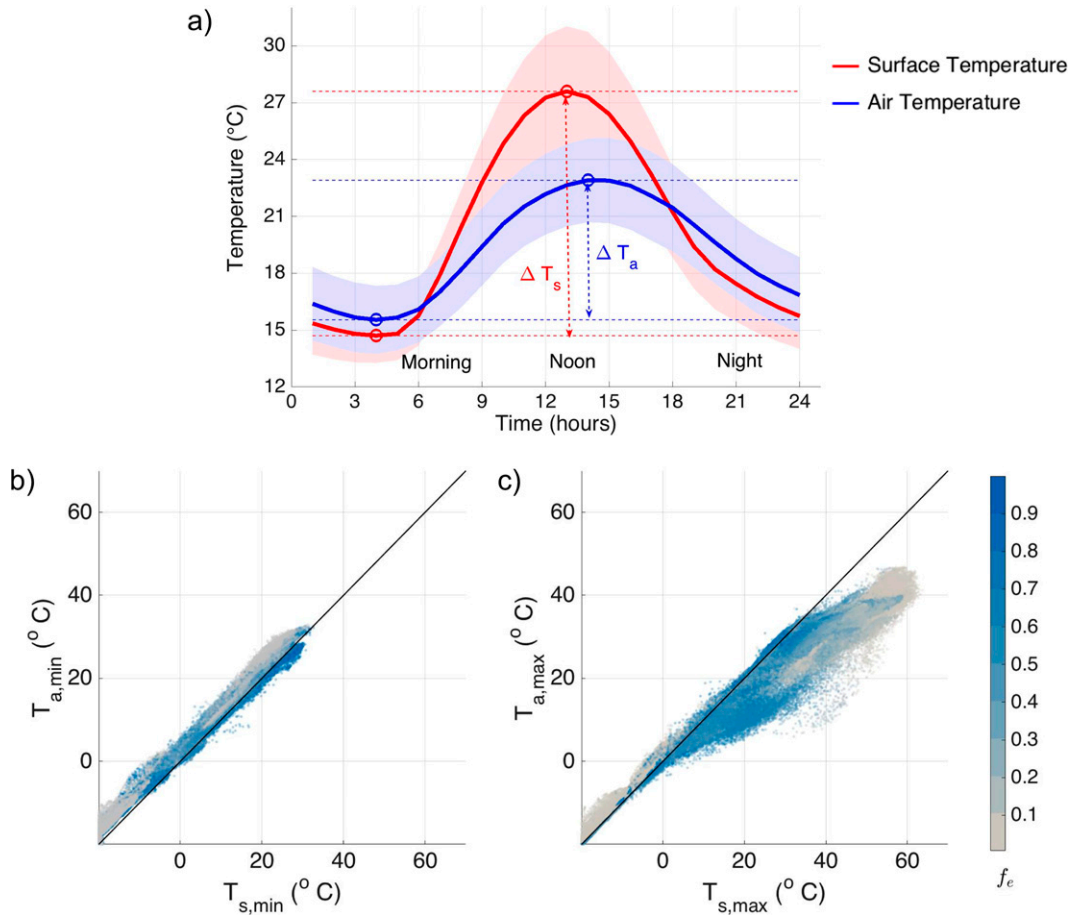Corresponding author: Annu Panwar, apanwar@bgc-jena.mpg.de

Fig. 1. (a) Mean diurnal variation of surface and air temperature for the summer season over the land surface in the ERA5 reanalysis (2000–15). The shaded regions show the standard error of the means. (b) The relationship between daily values of minimum surface ($T_{s,\min}$) and minimum air ($T_{a,\min}$) temperatures over the land surface in ERA5. (c) The relationship between daily maximum surface ($T_{s,\max}$) and maximum air ($T_{a,\max}$) temperatures over the land surface in ERA5. The color bar shows the mean evaporative fraction [$f_e = \mathrm{LE}/(\mathrm{LE} + H)$].

The diurnal evolution (or diel cycle) of surface and air temperature is dominantly shaped by the variation in solar energy input, but their amplitudes, or DTR, might respond differently to evaporative conditions. To illustrate this, we show in Fig. 1a the mean diurnal variation of surface and air temperature for the summer months (June–August for the Northern Hemisphere and December–February for Southern Hemisphere) for vegetated areas in the global ERA5 reanalysis (Copernicus Climate Change Service 2019). Figure 1b shows that the minimum surface ($T_{s,\min}$) and air ($T_{a,\min}$) temperatures are similar irrespective of the evaporative fraction (f_e, the ratio of the latent heat flux to the total turbulent heat flux). This is likely due to the absence of turbulent fluxes in the morning, although the latent heat release from dew formation might play a role in warming the minimum temperatures (Bourque and Arp 1994). The maximum surface temperature ($T_{s,\max}$), however, tends to be greater than the maximum air temperature ($T_{a,\max}$) on days with lower evaporative fraction (dry conditions) and to be more similar on the days with higher evaporative fraction (wet conditions), as shown in Fig. 1c. Since evaporation on land

occurs mainly during the daytime, the impact of evaporative cooling reduces the variation of daytime temperature. Hence, the effect of evaporative cooling can be quantified as the change in DTR from dry to wet conditions. In this study we quantify this reduction in ΔT_s and ΔT_a in response to evaporative fraction and examine the physical controls to obtain an explanation for the dominant processes shaping this reduction.

We also seek to explain the first-order responses of the diurnal temperature ranges using simple physical models to identify the major controls. Our previous study used a simple heat storage model (Panwar et al. 2019) to show that the diurnal warming rate of air temperature is strongly affected by the growth of the planetary boundary layer (PBL). Thus, the diurnal amplitude of air temperature could only be as high as the diurnal amplitude of surface temperature if the PBL height does not respond to the sensible heat flux. We then found that the weak response of air temperature to evaporative fraction in observations of a cropland site was due to the compensating effect of stronger boundary layer growth for drier conditions. In this study the warming rate is translated into

ΔT_a and then its relationship to boundary layer heat storage is obtained, primarily in the context of changing evaporative conditions. The heat storage in the boundary layer is calculated based on the maximum power limit (Kleidon and Renner 2017). The role of boundary layer growth on ΔT_a is accounted for by the lapse rate of potential temperature in the free atmosphere. We then investigate if these responses are independent of vegetation types and how they vary with energy availability for instance, from the tropics to extratropics.

Unlike air temperature, the diurnal variation of surface temperature is strongly governed by surface properties and its response to evaporative conditions can vary across vegetation types. Our recent study (Panwar et al. 2020), based on FLUXNET observations, shows that evaporation reduces ΔT_s similarly across vegetation types. In forests, however, the cooling due to their high aerodynamic conductance is more dominant, thus reducing the sensitivity to evaporative conditions. These findings were established using a surface energy balance–based expression of ΔT_s. Here, we further simplify and develop this approach in order to capture the role of solar radiation, aerodynamic conductance, and evaporative fraction in explaining the spatial variation in ΔT_s across FLUXNET sites and across continents in ERA5. Even though the FLUXNET and ERA5 datasets represent quite different scales, we argue that the main drivers in shaping diurnal temperature variations and its buffering in the lower atmosphere are the same (as shown in our previous studies). Because these drivers are to first order independent of scale, we should find similar functional responses at local FLUXNET sites and at the coarser, corresponding grid cell in the ERA5 reanalysis. The sensitivities of ΔT_s and ΔT_a to evaporative fraction and vegetative cover should then also be similar and explainable by the same physical constraints.

To conduct this study, we use FLUXNET observations (Pastorello et al. 2020) across different vegetation types and the global ERA5 reanalysis (Copernicus Climate Change Service 2019). Both data sources have their benefits and drawbacks. FLUXNET provides in situ observations of near-surface meteorological variables but does not provide PBL height (Helbig et al. 2020). ERA5 provides information on PBL development that is required to explore the role of PBL dynamics in shaping ΔT_a, but it is a modeled product. To identify potential biases, we compare the DTR responses to evaporative fraction in both datasets. The cooling effect of evaporation is expected for conditions that are not energy limited. Finally, we aim to extend our insights from the FLUXNET observations to the continental scale as well as to boundary layer dynamics by the combination of both data sources.

In the following section we present two simple models that explain the physical constraints of ΔT_a and ΔT_s. The formulation of ΔT_a uses a simple PBL heat storage approach based on Panwar et al. (2019), and the formulation of ΔT_s uses a simple surface energy balance model based on Panwar et al. (2020). After describing the data sources and their preparation, we analyze and compare the ΔT_a and ΔT_s responses to evaporative fraction in FLUXNET and ERA5 in the results section. There, we also demonstrate how well our simple models can reproduce the geographical variation of ΔT_a and ΔT_s responses to evaporative fraction across vegetation types

and across different climates. We then discuss and conclude with the implications of our study for a better understanding of land–vegetation–atmosphere interactions.

2. Methods

The diurnal variation of surface and air temperature is driven by absorbed solar radiation (R_s) and its partitioning into latent (LE) and sensible (H) heat flux. In this section we formulate ΔT_a and ΔT_s, starting from the surface energy balance that is given as

$$R_s + R_{l,\text{net}} = \text{LE} + H + G. \qquad (1)$$

Here, $R_{l,\text{net}}$ is the net longwave radiation and G is the ground heat flux. For simplification, diurnal changes in G are neglected (e.g., Betts and Ball 1995). The heat discharged from the surface cools the surface but contributes to the increase in heat storage in the atmospheric boundary layer.

We first use the components of the surface energy balance to formulate energy storage changes in the boundary layer, from which we infer ΔT_a. We refer to this model for ΔT_a as the simple atmospheric boundary layer (SABL) model. We then derive an expression for ΔT_s by solving the surface energy balance for surface temperature, using a few simplifications. We refer to this model for ΔT_s as the simplified surface energy balance (SSEB) model.

a. Formulating the ΔT_a response to evaporative fraction using SABL

Over land, the diurnal variation of air temperature ΔT_a reflects mostly the heat storage change (ΔU) in the lower atmosphere due to strong variation in solar radiation. Part of the absorbed solar radiation is utilized in evaporation and does not contribute to a rise in air temperature. The increase in boundary layer heat storage is thus approximately given by $d(\Delta U)/dt = R_s - \text{LE}$. We use this energy balance constraint (Kleidon and Renner 2017) and the maximum power limit for turbulent fluxes (Kleidon and Renner 2018) to obtain the relationship of ΔU and evaporative fraction (f_e; see appendix B for the derivation):

$$\Delta U = \frac{2 - f_e}{2 + f_e} \Delta U_0. \qquad (2)$$

Here, ΔU_0 is the heat storage variation in the absence of evaporation, which depends on absorbed solar radiation and daylight length (Δt_{day}) by $\Delta U_0 = R_{s,\text{avg}}\Delta t_{\text{day}}$, or, rewritten in terms of maximum solar radiation ($R_{s,\text{max}}$), as $\Delta U_0 = (2R_{s,\text{max}}\Delta t_{\text{day}})/\pi$.

The diurnal temperature range ΔT_a directly relates to this heat storage change, but the amplitude also depends on the PBL height. Figure 2a shows a simple depiction of the PBL heat storage and how it relates to ΔT_a for dry (orange) and wet (blue) conditions. The heat storage change is represented by the triangle, whose y axis is the boundary layer height (Δz) and the x axis is the change in potential temperature (θ). Generally, the 2-m air temperature is similar to the potential
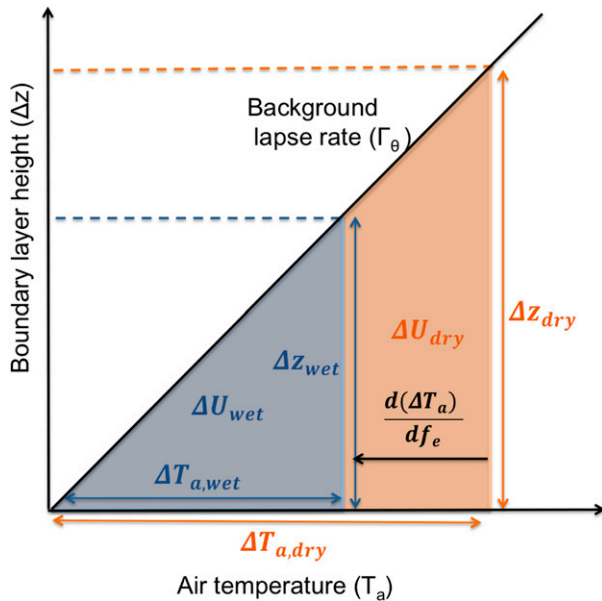
FIG. 2. A conceptual illustration of the heat storage change ΔU in the atmospheric boundary layer (colored areas) in relation to the diurnal temperature range ΔT_a and the change in boundary layer height Δz for a given background lapse rate in potential temperature Γ_θ. Two cases are shown for wet (blue) and dry (orange) evaporative conditions.

temperature (Stull et al. 2015), so we can assume that the morning to afternoon change in PBL potential temperature is equivalent to ΔT_a. For dry conditions, both ΔU and Δz increase in response to stronger buoyancy due to a higher sensible heat flux and less latent heating. In contrast, for wet conditions (blue triangle) Δz and ΔU are lower, resulting in a lower response in ΔT_a. The difference between the dry and wet ΔT_a depicted in the x axis is a measure of the evaporative cooling effect of ΔT_a that is expressed as $d(\Delta T_a)/df_e$.

We can thus express ΔU in terms of ΔT_a and the planetary boundary layer height Δz by [following Panwar et al. (2019)]

$$\Delta U = c_p \rho \Delta T_a \frac{\Delta z}{2}. \tag{3}$$

Here $c_p = 1005$ J kg^{-1} is the specific heat capacity and ρ is the density of air. Note that the air density changes with elevation but for simplification we consider a constant value of $\rho = 1.23$ kg m^{-3}.

During the day, the boundary layer height grows as per the background lapse rate of potential temperature (Γ_θ). When we assume that Γ_θ is similar for dry and wet conditions, we can write $\Delta z = \Delta T_a/\Gamma_\theta$. Using Γ_θ and Eq. (2) for ΔU, we can then express ΔT_a as

$$\Delta T_a = \left(\frac{2 - f_e}{2 + f_e}\right)^{1/2} \Delta T_{a0}. \tag{4}$$

Here ΔT_{a0} is the ΔT_a in the absence of evaporation that depends on solar radiation, background lapse rate, and

daylight length, given by $(\Delta T_{a0})^2 = (2\Gamma_\theta R_{s,\max}\Delta t_{\text{day}})/(\pi c_p \rho)$. By taking the derivative of Eq. (4) with respect to f_e we get the response of ΔT_a to a change in evaporative fraction:

$$\frac{d(\Delta T_a)}{df_e} = -\frac{2}{[(2 - f)_e/(2 + f_e)]^{1/2}(2 + f_e)^2}\Delta T_{a0} \approx -0.4\Delta T_{a0}. \tag{5}$$

Note that this expression hardly depends on f_e, because the denominator in Eq. (5) varies only weakly from 4 for $f_e = 0$ to 5.2 for $f_e = 1$. The negative sign of $d(\Delta T_a)/df_e$ shows that ΔT_a decreases with greater evaporative fraction. This decrease is up to 40% of ΔT_{a0} over the range from $f_e = 0$ to $f_e = 1$. Because ΔT_{a0} depends on $R_{s,\max}$, ΔT_{a0} as well as $d(\Delta T_a)/df_e$ increase in regions with higher solar energy input. However, when calculating this sensitivity one needs to consider potential variations in Γ_θ.

b. Formulating the ΔT_s response to evaporative fraction using SSEB

The diurnal variation in surface temperature, ΔT_s, mainly depends on the absorbed solar radiation, R_s, and its partitioning into surface energy balance components. It can be derived by linearizing net longwave radiation, expressing the latent heat flux by the evaporative fraction, and by expressing the sensible heat flux in terms of an aerodynamic conductance g_a (Panwar et al. 2020). Then, the diurnal change in surface temperature in response to R_s can be expressed as

$$\frac{dT_s}{dR_s} \approx \frac{dT_a}{dR_s} + \frac{1 - f_e}{c_p \rho g_a} - \frac{\overline{(T_s - T_a)}}{g_a}\frac{dg_a}{dR_s}. \tag{6}$$

Here, $\overline{T_s - T_a}$ is the morning time mean of the difference between surface and air temperature. The aerodynamic conductance, g_a, depends on vegetation type and its sensitivity to solar radiation is expressed as dg_a/dR_s. Note that the warming rates for surface and air temperature, dT_s/dR_s and dT_a/dR_s, are related to each other and are more similar for higher values of f_e and lower values of $\overline{T_s - T_a}$. On integrating Eq. (6) over the morning from $R_s = 0$ to $R_s = R_{s,\max}$, we get the expression for ΔT_s as follows:

$$\Delta T_s = \Delta T_a + \frac{(1 - f_e)}{c_p \rho \overline{g_a}}R_{s,\max} - \frac{\Delta g_a}{\overline{g_a}}\overline{(T_s - T_a)}. \tag{7}$$

Here Δg_a is the morning to afternoon increase in aerodynamic conductance. Integrating dT_s/dR_s to obtain ΔT_s is an approximation since $T_{s,\max}$ and $R_{s,\max}$ occur at a similar time during the day. The diurnal temperature range for air temperature, ΔT_a, however, reflects a somewhat different integration because the maximum air temperature occurs in the afternoon (after $R_s = R_{s,\max}$; see also Fig. 1a). Hence, assuming that $(dT_a/dR_s)R_{s,\max} \approx \Delta T_a$ can lead to slight underestimation of ΔT_a.

Equation (7) can further be simplified by assuming that $T_{s,\min} \approx T_{a,\min}$ (see Fig. 1b), such that ΔT_s can be expressed as $\Delta T_s = \Delta T_a + T_{s,\max} - T_{a,\max}$. Figure A1 in appendix A shows
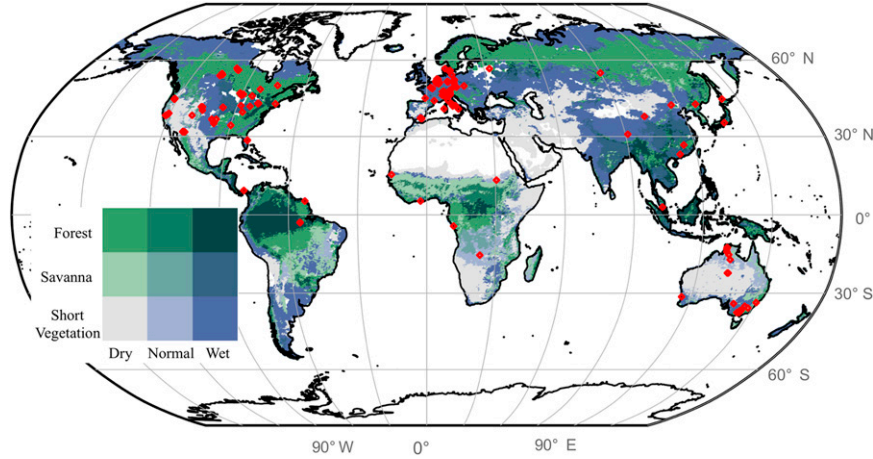
FIG. 3. Location of FLUXNET sites (red symbols) used for this study in relation to the vegetation type (green shades) and mean evaporative conditions (blue shades). The vegetation type is based on the IGBP classification. The mean evaporative conditions are defined as dry ($f_e \leq 0.35$), normal ($0.35 < f_e \leq 0.65$), and wet ($0.65 < f_e < 1$) and are obtained from the ERA5 reanalysis (2000–15).

that $T_{s,\max} - T_{a,\max} \approx 1.4(\overline{T_s - T_a})$. Based on these simplifications, we get ΔT_s as follows:

$$\Delta T_s \approx \Delta T_a + \frac{1.4(1 - f_e)}{c_p \rho(1.4\overline{g_a} + \Delta g_a)} R_{s,\max}. \qquad (8)$$

To get the response of ΔT_s to evaporative fraction, we take the derivative of Eq. (8) with f_e such that

$$\frac{d(\Delta T_s)}{df_e} \approx \frac{d(\Delta T_a)}{df_e} - \frac{1.4}{c_p \rho(1.4\overline{g_a} + \Delta g_a)} R_{s,\max}. \qquad (9)$$

Equation (9) suggests that the sensitivity of $d(\Delta T_s)/df_e$ mainly depends on solar radiation, $R_{s,\max}$, and aerodynamic conductance, g_a, which depends on vegetation type, as we will see below. Since $d(\Delta T_a)/df_e$ as well as the second term of Eq. (9) is negative, $d(\Delta T_s)/df_e$ is also negative. Or, in other words, ΔT_s decreases with an increase in evaporative fraction. Additionally, $d(\Delta T_s)/df_e$ increases in regions with higher solar radiation.

3. Data

To evaluate the DTR responses to evaporative fraction, we use temperatures and surface energy balance components from FLUXNET observations and ERA5 reanalysis. The global FLUXNET network provides routine observations of local atmospheric state variables and surface energy balance components using the eddy covariance technique (Pastorello et al. 2020). Here, data from 160 FLUXNET sites with short vegetation (63), savanna (20), and forest (77) with observations for more than 2 years are used. Land cover types are assigned based on the International Geosphere–Biosphere Programme (IGBP) classification, as in Falge et al. (2017a). Short vegetation consists of croplands, grasslands and shrublands, and forest consists of mixed forest, deciduous, evergreen,

broadleaf, and needleleaf forests. Please refer to Table A1 in appendix A for site-specific land cover types. Figure 3 depicts the geographical locations of the FLUXNET sites used here, with the detailed description of each site provided in Table A1.

The FLUXNET data used in this study are gap-filled with the multidimensional scaling (MDS) method as described in Reichstein et al. (2005). Medium- to poor-quality gap-filled data are rejected and only measured and good quality gap-filled data are considered in this study. A more detailed description of the FLUXNET dataset processing is available at Pastorello et al. (2020).

Furthermore, we use the fifth-generation ERA5 reanalysis product by the European Centre for Medium-Range Weather Forecasts (ECMWF) (Copernicus Climate Change Service 2019) at a spatial resolution of 31 km ($0.25°$ latitude–longitude grid) for the years 2000–15. We primarily use the temperature products as well as the boundary layer height product of the ERA5 reanalysis that is required to evaluate Γ_θ and thereby the ΔT_a response to evaporative fraction. Additionally, in order to identify and understand the biases between FLUXNET and ERA5, we compare DTR responses to evaporative fraction in ERA5 with the grid cells covering the FLUXNET sites. We then attribute possible biases to differences in the surface energy balance.

The responses of ΔT_s and ΔT_a to evaporative fraction from FLUXNET and ERA5 are obtained from the slope of their linear regressions against evaporative fraction that we describe as $d(\Delta T_s)/df_e$ and $d(\Delta T_a)/df_e$, respectively. In case of FLUXNET, we obtain these slopes as per vegetation type, using daily observations of DTR and f_e. In case of ERA5, we quantify ΔT_s and ΔT_a responses to evaporative fraction locally (i.e., at each grid cell), globally (i.e., by combining all vegetated land grid cells), and at FLUXNET sites. The ERA5 local response are based on daily values at each grid point,
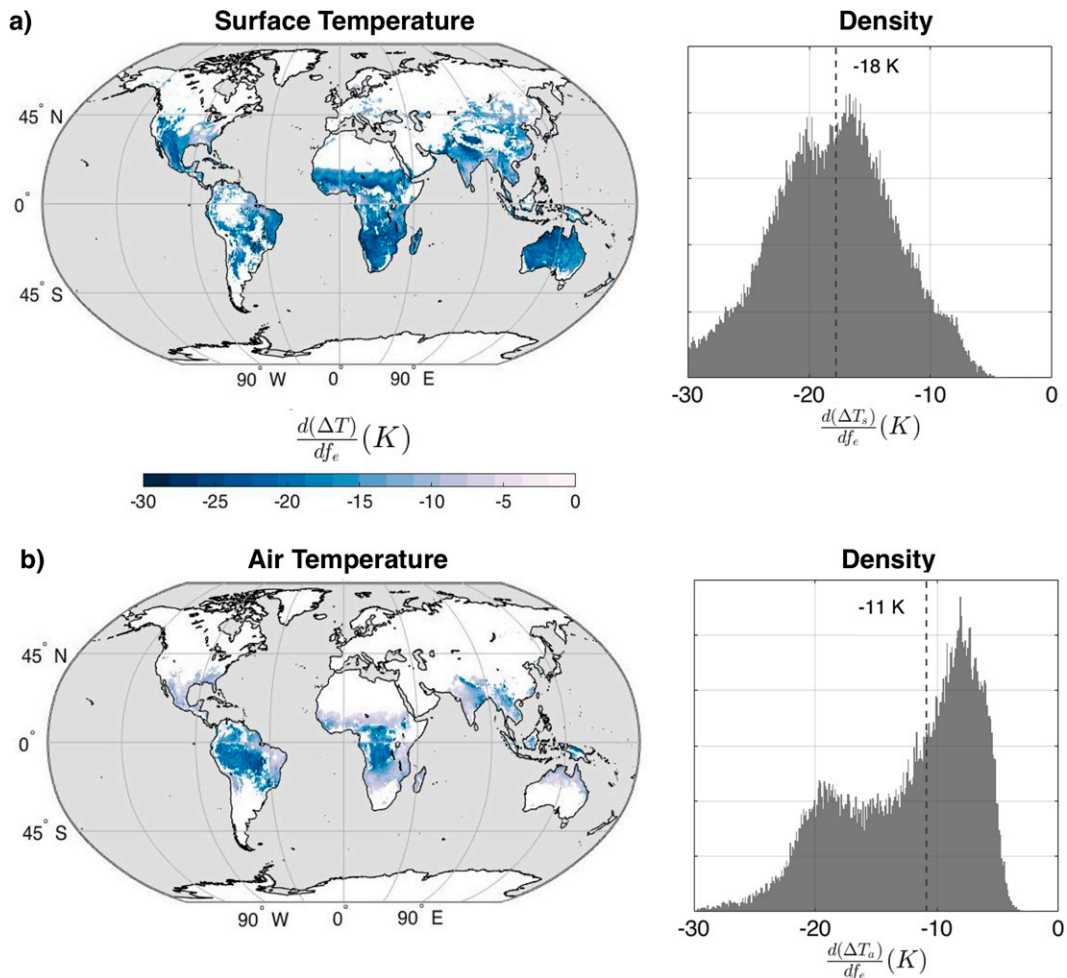
FIG. 4. Local responses of (a) ΔT_s and (b) ΔT_a to evaporative fraction obtained from the daily values of the summer season in ERA5 reanalyses for the years 2000–15. Only grid cells with $R^2 > 0.3$ for the regression of ΔT_a and f_e are shown. The histograms show the density distribution of these responses with the median values indicated by the dashed lines.

and their analysis is aimed to identify regions with significant responses. Considering that not all the regions have a sufficiently large range in evaporative fraction, weaker and insignificant responses in those regions are expected. The limited range in evaporative fraction can be addressed by simply exploiting the natural occurrence of vegetation in different mean evaporative conditions. This is illustrated in Fig. 3, where the mean evaporative fraction is classified into three ranges for simplicity, as dry ($f_e \leq 0.35$), normal ($0.35 < f_e \leq 0.65$), and wet ($0.65 < f_e < 1$). In the global analysis we utilize this spatial combination of vegetation type and their mean evaporative fraction. Last, to compare the results from FLUXNET and ERA5, we estimate $d(\text{DTR})/df_e$ using the daily values of DTR and f_e of the ERA5 grid points covering the FLUXNET sites.

We consider only time periods with non-energy-limited conditions to avoid the positive relationship of temperature and evaporation (Garcia et al. 2014; Sun et al. 2016) and to select days with a well-mixed convective boundary layer. We

selected summer days corresponding to June, July, and August (JJA) in the Northern Hemisphere and December, January, and February (DJF) in the Southern Hemisphere. Likewise, in ERA5, we only consider latitudes inside 66°S–66°N. In FLUXNET as well as in ERA5, air temperature is the temperature ~2 m above the ground or canopy. Since FLUXNET does not provide direct observations of surface temperature, we obtain it from the surface upwelling flux of longwave radiation using the Stefan–Boltzmann law. It should be noted that surface emissivity varies with surface moisture, vegetation, composition, and roughness, usually ranging from 0.8 to 1 (Humes et al. 1994; Valor and Caselles 1996; Nerry et al. 1988; Thome 2014). For simplicity we used a surface emissivity of 1. Surface temperature in ERA5 is available as skin temperature that is derived from the surface energy balance (ECMWF 2007). Additionally, daily minimum and maximum temperatures and DTR are calculated based on the half-hourly and hourly values in FLUXNET and ERA5, respectively. More information on the calculation of
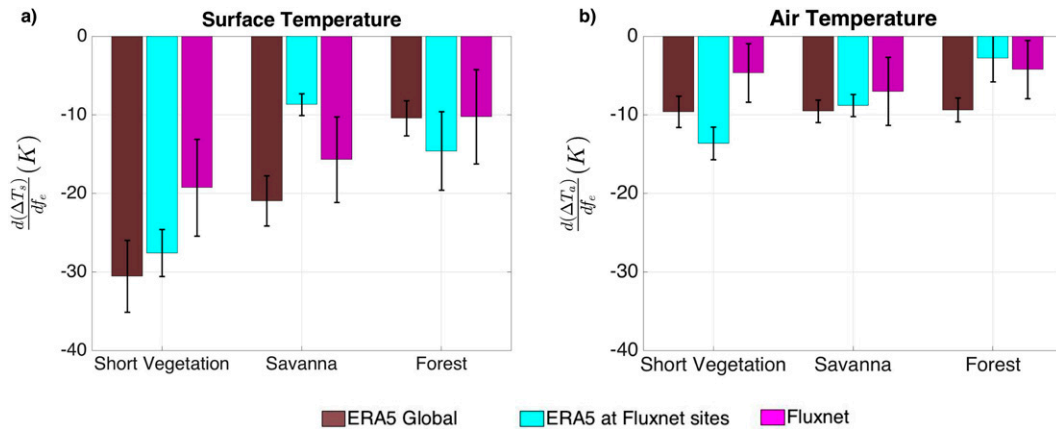
FIG. 5. Bar plots of (a) ΔT_s and (b) ΔT_a responses to evaporative fraction in ERA5 and FLUXNET for short vegetation, savanna, and forests. The ERA5 global estimate (brown bars) is obtained from all grid points falling into the respective vegetation type (except high latitudes). The cyan bars show the estimate obtained from ERA5 reanalyses at FLUXNET sites and the magenta bars using FLUXNET observations. The error bars represent the root-mean-square error for the respective estimates. The median values and regression statistics of these estimates are provided in Table 1.

different variables of FLUXNET and ERA5 is provided in Table A2 of appendix A.

The influence of vegetation type on ΔT_s and ΔT_a responses to evaporative fraction is evaluated through their aerodynamic conductance (g_a). To maintain consistency with the surface energy balance, the aerodynamic conductance is obtained from the observed sensible heat flux (H), such that $g_a = H/[c_p\rho(T_s - T_a)]$. Because g_a is also sensitive to absorbed surface solar radiation (R_s) (Kumagai et al. 2004), we have also calculated the change in aerodynamic conductance (Δg_a) from morning ($R_s = 10$ W m^{-2}) to solar noon ($R_s = R_{s,\max}$) at FLUXNET sites.

4. Results

We start the presentation of the results with documenting the responses of the diurnal temperature ranges to evaporative fraction in ERA5 and FLUXNET and compare these to identify

potential biases. We then use the models presented in section 2 to explain the responses of ΔT_a and ΔT_s separately. We recommend using our models mainly to evaluate surface and air temperature responses to evaporative conditions. Figure A2 in appendix A shows our models' performance in estimating diurnal range of surface and air temperature. The consistent underestimation of the diurnal temperature range occurs because of some simplified assumptions that are discussed in the method sections.

a. The DTR responses to evaporative fraction in ERA5 and FLUXNET

Figures 4a and 4b show the local $d(\Delta T_s)/df_e$ and $d(\Delta T_a)/df_e$ obtained from the ERA5 reanalysis for summer months. These local responses are calculated from the linear regression of the daily values of ΔT and evaporative fraction (with a total of 1350 days) at each grid point for vegetated surfaces. We find that ΔT_s reduces more strongly than ΔT_a in response to higher

TABLE 1. The median values of $d(\Delta T_s)/df_e$ and $d(\Delta T_a)/df_e$ obtained from the global ERA5 reanalyses, ERA5 reanalyses at FLUXNET sites, and FLUXNET observations.

|	$d(\Delta T_s)/df_e$ (K)			$d(\Delta T_a)/df_e$ (K)		
Vegetation	ERA5 Global	ERA5 at FLUXNET sites	FLUXNET	ERA5	ERA5 at FLUXNET sites	FLUXNET
Short vegetation	−30.56	−27.60	−19.28	−9.62	−13.65	−4.65
R^2	0.64	0.60	0.28	0.49	0.42	0.06
RMSE	4.56	3.00	6.15	1.98	2.08	3.72
Savanna	−21.00	−8.70	−15.88	−9.55	−8.83	−7.03
R^2	0.46	0.56	0.25	0.47	0.56	0.12
RMSE	3.20	1.40	5.43	1.43	1.40	4.25
Forest	−10.44	−14.60	−10.25	−9.38	−2.80	−4.24
R^2	0.26	0.44	0.10	0.39	0.08	0.04
RMSE	2.24	5.00	6.00	1.51	3.00	3.71
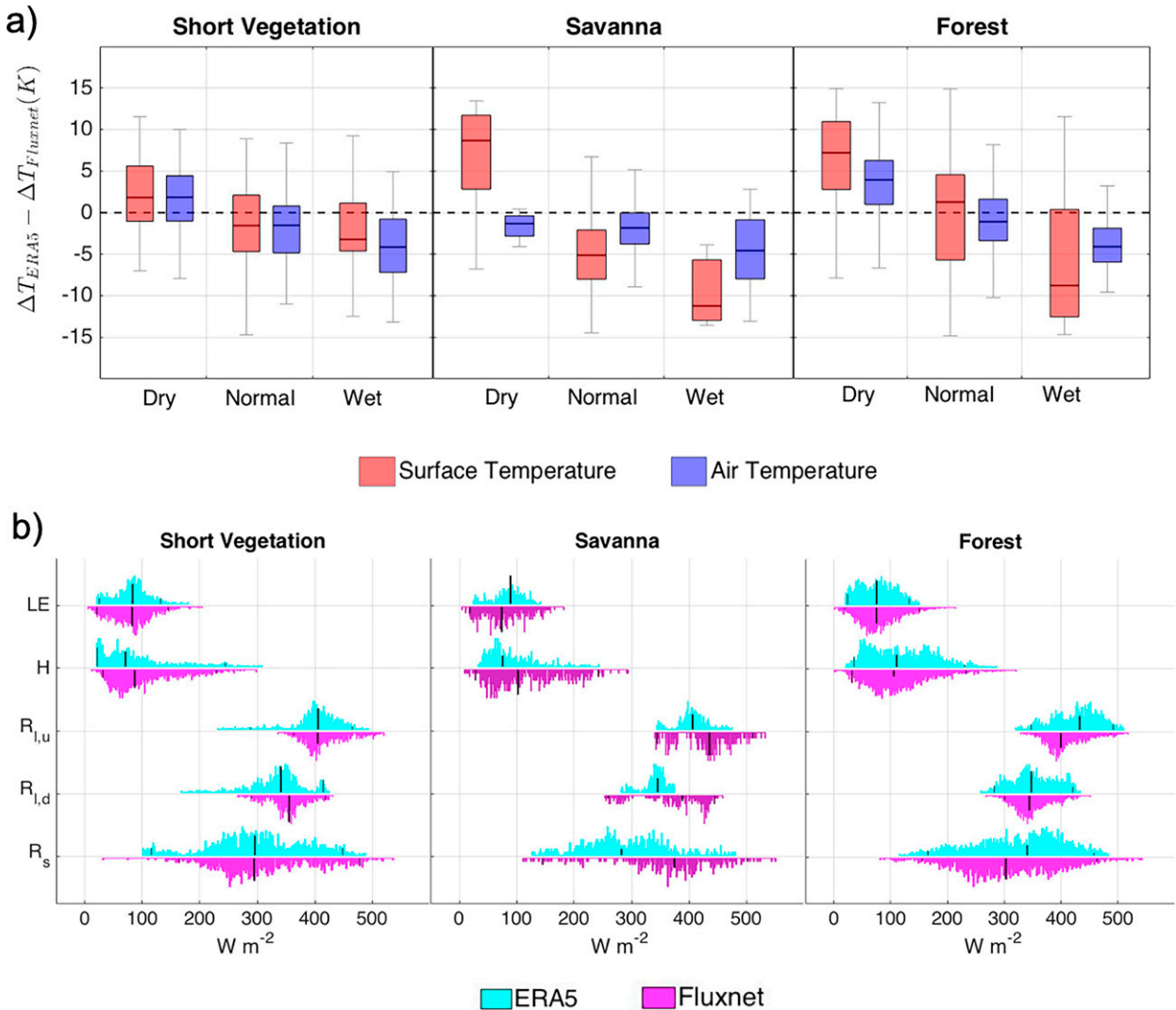
FIG. 6. Biases in ERA5 (a) diurnal temperature ranges and (b) surface energy balances in comparison to FLUXNET observations. The bias in the diurnal temperature range is expressed by the difference between the ERA5 and the FLUXNET values, separately for short vegetation, savanna, and forests for dry, normal, and wet conditions. The density plot of the surface energy balance components shows the latent (LE) and sensible (H) heat fluxes, upwelling ($R_{l,u}$) and downwelling ($R_{l,d}$) longwave radiation, and absorbed solar radiation (R_s) for ERA5 (cyan) and FLUXNET (magenta) for short vegetation, savanna, and forests. The nearest ERA5 grid points to the FLUXNET locations are used.

evaporative fractions. The frequency distribution of these responses shows a decrease in ΔT_s by 18 K (median) and in ΔT_a by 11 K (median) in response to an increase in evaporative fraction. Here only regions with correlation coefficients higher than $R^2 > 0.3$ for the regression between ΔT and f_e are shown. Local responses are sensitive to the range of evaporative fraction, which in turn depends on soil moisture dynamics and solar radiation (Nutini et al. 2014; Wang and Dickinson 2012). Consequently, the regression to estimate $d(\Delta T)/df_e$ is much more significant in the regions where evaporative fraction is variable (see Fig. A3). Additionally, these responses might vary across vegetation types, an aspect that we explore further and compare with FLUXNET data.

An alternative approach to obtain $d(\Delta T)/df_e$ is to simply utilize the existing spatial variation in vegetation and evaporative fraction that is shown in Fig. 3, using the summertime mean values. We refer to this estimate as the ERA5 global estimate. Figures 5a and 5b display $d(\Delta T_s)/df_e$ and $d(\Delta T_a)/df_e$ derived from the ERA5 reanalysis along with that from the FLUXNET observations for short vegetation, savanna, and forests. The responses derived from ERA5 are shown in terms of the global estimate (brown) as well as at FLUXNET sites (cyan), that uses only the grid cells closest to or at the FLUXNET sites. Despite the fact that surface and air temperature are closely related, their diurnal ranges respond remarkably different to evaporative fraction. Figure 5a shows that
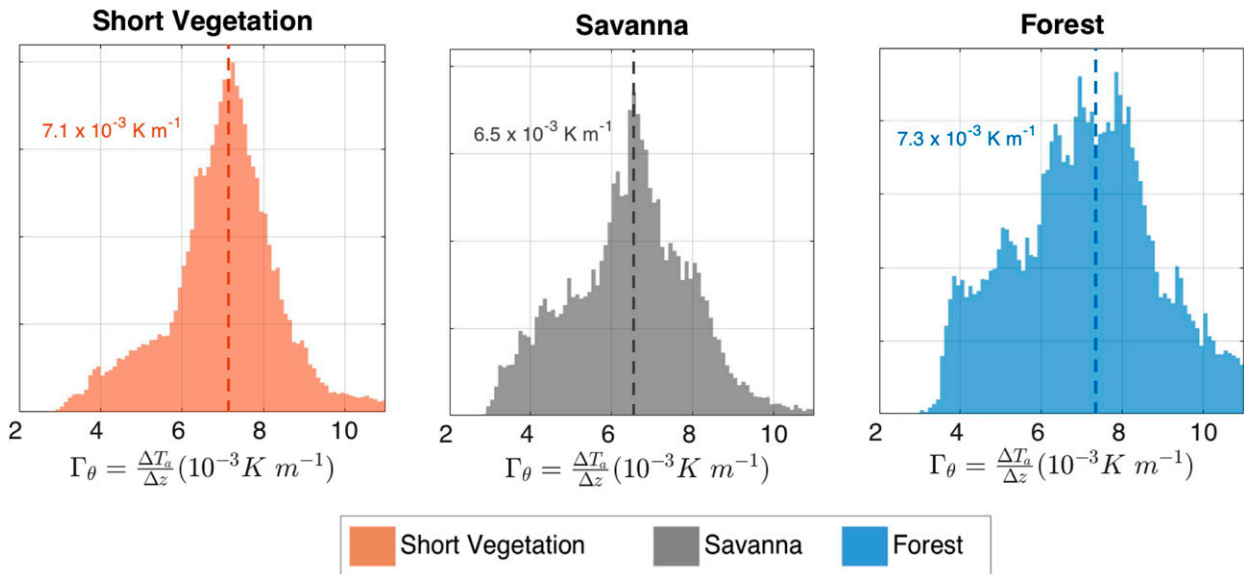
FIG. 7. The density distributions of the background lapse rate of potential temperature ($\Gamma_\theta = \Delta T_a / \Delta z$) in short vegetation, savanna, and forests obtained from ERA5 reanalyses. The dashed lines show the median values of the distribution that is also indicated in the figures.

$d(\Delta T_s)/df_e$ strongly differs among vegetation types, being higher in short vegetation (≈ -20 K in FLUXNET, -30 K in ERA5) and lower in forests (≈ -10 K in FLUXNET and ERA5). However, $d(\Delta T_a)/df_e$ is much lower than $d(\Delta T_s)/df_e$ and remains almost similar (≈ -5 K in FLUXNET and -10 K in ERA5) across vegetation types. Table 1 summarizes the statistics of $d(\Delta T_s)/df_e$ and $d(\Delta T_a)/df_e$ shown in Fig. 5.

Overall, the responses of ΔT to evaporative fraction in ERA5 and FLUXNET show similar patterns, even though these responses appear to be consistently stronger in ERA5 than in FLUXNET. This is mainly true for the ERA5 global responses that are more significant than the responses at FLUXNET sites, presumably due to larger data and a higher range in evaporative fraction. Additionally, this stronger response in ERA5 might result from systematic biases in the surface energy balance components that affect the ΔT responses.

To examine the disparity between the DTR responses in ERA5 and FLUXNET further, we directly look at the differences in ΔT in ERA5 at FLUXNET sites (Fig. 6a). These biases are obtained monthly and are aggregated based on the evaporative conditions, dry, normal, and wet, respectively. In general, ERA5's ΔT is higher in dry and lower in wet conditions when compared to FLUXNET observations. In short vegetation, ERA5 ΔT_s are slightly higher by ≈ 2 K for dry conditions and considerably lower by ≈ 4 K for wet conditions. When combined, these biases can explain the overestimation of $d(\Delta T_s)/df_e$ by ≈ 8 K in ERA5 at FLUXNET sites (Fig. 5a). Similar biases in savanna are observed that explain the stronger ERA5 global ΔT response than in FLUXNET observations. However, it does not explain the lower ERA5 responses at FLUXNET sites. This may be because savannas are exceptionally heterogeneous, which causes high variability in temperatures between tree canopies and the surrounding open

land surface and hence a greater uncertainty in observations (Trigo et al. 2008, 2011; Ermida et al. 2014). Moreover, inaccuracies in vegetation cover in ERA5 can result in significant biases in diurnal temperature variations (Johannsen et al. 2019; Wang and Prigent 2020). In forests, ΔT_s in ERA5 on dry days is higher by ≈ 7 K and lower by ≈ 10 K on wet days than in FLUXNET observations that fairly explains the bias of $d(\Delta T_s)/df_e$ in ERA5 at FLUXNET sites. Similar biases are observed for ERA5's ΔT_a, as shown in Fig. 6a, although these biases cannot be seen in the mean response in ERA5 at FLUXNET sites (see Fig. 5b). Overall, it appears that the ERA5 reanalysis overestimates the sensitivity of ΔT_a to evaporative conditions.

As shown in Fig. 6a, ERA5 has a systematic positive ΔT bias for dry conditions and negative bias for wet conditions. To find the sources of these biases, we compare the associated surface energy balance components for the summer months between ERA5 and FLUXNET in Fig. 6b. In short vegetation, overall ERA5's ΔT is lower than FLUXNET's ΔT, which is also evident in comparatively lower values of sensible heat flux in ERA5. Similarly, in savanna ERA5's ΔT is overall considerably lower than FLUXNET's ΔT, but in this case lower R_s in ERA5 appears to be the main cause for the lower ERA5's ΔT. In forests, however, R_s is higher in ERA5 than in FLUXNET, but this does not lead to an overall positive bias in ΔT, although it might explain the positive bias for dry conditions. The comparison of surface energy components does not directly convey the explicit source for the ΔT biases yet could be useful to understand how these biases in surface energy components propagate to biases in diurnal temperatures through inaccurate representation of surface process. In ERA5 the surface energy balance is satisfied by calculating surface temperature with a similar approach to the Penman–Monteith (Brutsaert 2013) and Best et al. (2004) methods. Here we use ERA5 fluxes accumulated hourly, which may be
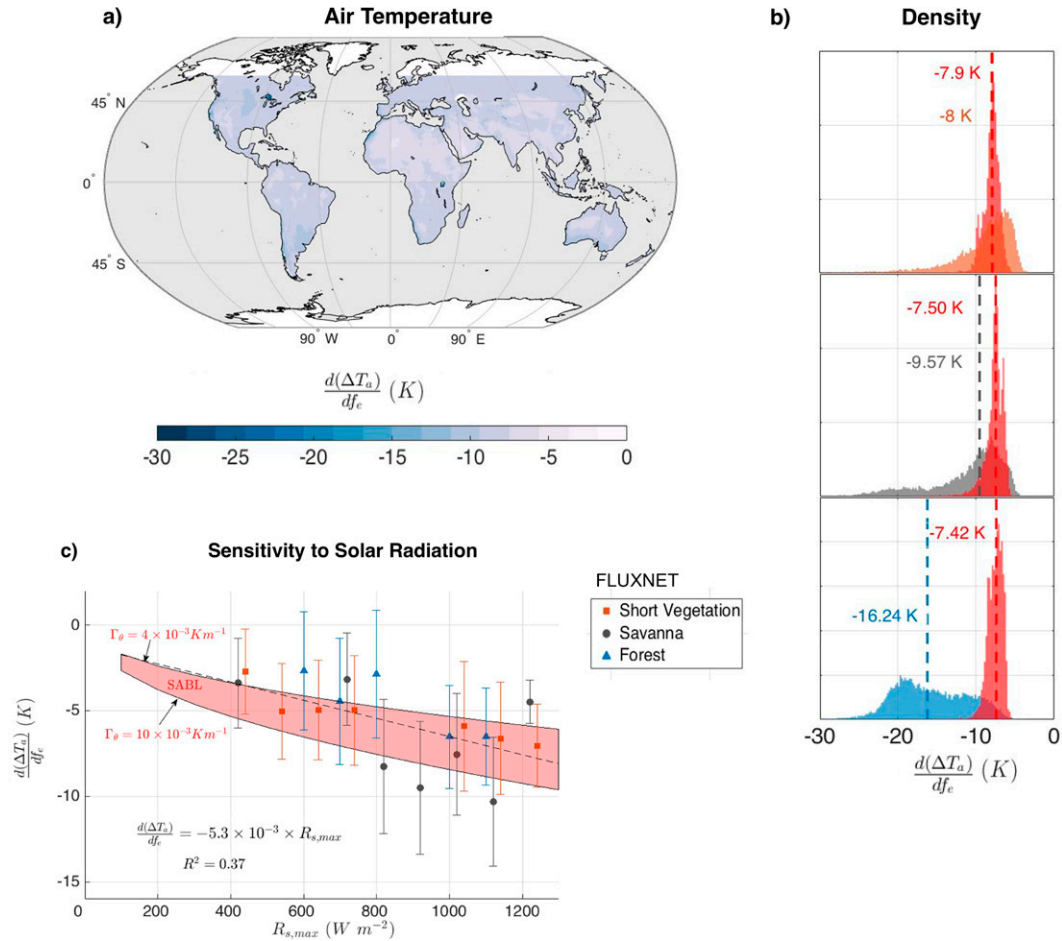
FIG. 8. The response of ΔT_a to evaporative fraction estimated from our SABL model using values of $\Gamma_\theta (\Delta T_a/\Delta z)$ and $R_{s,\max}$ from ERA5 in terms of (a) its mean geographic distribution, (b) its density distribution (red) compared to the one obtained from ERA5 for short vegetation, savanna, and forest (as shown in Fig. 4b), and (c) its sensitivity to maximum solar radiation $R_{s,\max}$ (red shaded area) compared to FLUXNET estimates for short vegetation, savanna, and forests. The dashed lines in (b) indicate the median values of the distribution. The error bars in (c) represent the RMSE and the black dashed line represents the linear regression of $d(\Delta T_a)/d(f_e)$ to $R_{s,\max}$.

different than the fluxes reported at FLUXNET sites due to solar zenith angle changes. Details of ERA5 model assimilation and physical parameterization (ECMWF 2007) are important when comparing ERA5 data to observations. The validation of the ERA5 reanalysis is not our primary objective, but it would seem that there are some systematic biases in the ERA5 surface energy balance components that would need to be considered when using and interpreting its temperature products, particularly when evaluating these in the context of water availability changes.

To summarize our ERA5- and FLUXNET-based findings, we found that even though diurnal surface and air temperature ranges are strongly related, they do not respond in the same way to evaporative fraction. Using FLUXNET observations and ERA5 reanalysis we find a strong decrease in ΔT_s in response to greater evaporative fraction, especially in short vegetation. ΔT_a has a weaker sensitivity to evaporative fraction that is similar across vegetation types. In the next two sections we use the physically

constrained models described in the Methods section (section 2) to reproduce and explain the ΔT_a and ΔT_s responses to f_e.

b. Explaining the ΔT_a response to evaporative fraction

We first use the model presented in section 2a to reproduce the low ΔT_a sensitivity to evaporative fraction that is similar across vegetation types. According to Eq. (3), ΔT_a depends mainly on the change in PBL height (Δz and Γ_θ), evaporative fraction (f_e), and heat storage (ΔU) from morning to afternoon, but the expression does not depend on vegetation type. This is consistent with our findings in the previous section. To solve for $d(\Delta T_a)/df_e$ [Eq. (5)], we require $R_{s,\max}$, Γ_θ, and Δt_{day}, which we obtain from the summer mean values from ERA5. Figure 7a shows the value of Γ_θ for short vegetation, savanna, and forest from $\Gamma_\theta = \Delta T_a/\Delta z$. We found that Γ_θ is similar across vegetation types with a median value of $\approx 7 \times 10^{-3}$ K m^{-1}, with some notable variation in values between 4 and 10×10^{-3} K m^{-1}.
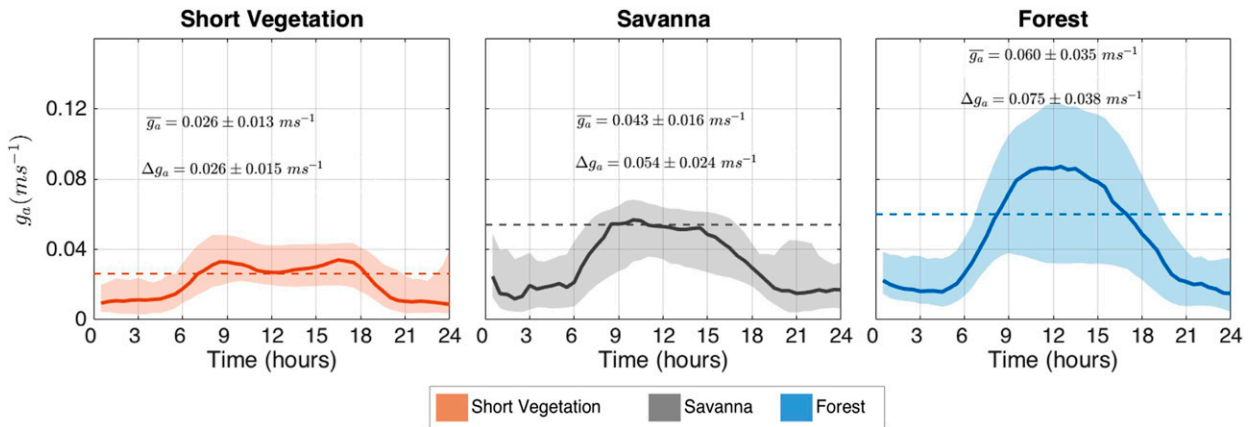
FIG. 9. The mean diurnal variation of aerodynamic conductance g_a in short vegetation, savanna, and forests at FLUXNET sites. The shaded areas represent the standard deviations of the mean. The dashed lines mark the morning to afternoon mean values. The value for the morning to afternoon change, Δg_a, is also provided for each vegetation type. The numbers provide the mean and standard errors for g_a and Δg_a.

We next use local values of Γ_θ obtained from ERA5 in our SABL model to reproduce $d(\Delta T_a)/df_e$ for each grid point.

Figure 8a shows that $d(\Delta T_a)/df_e$ obtained using the SABL model is reasonably invariant with a median value of -8 K, which is comparable to ERA5 (Fig. 4b). Likewise, the distributions of $d(\Delta T_a)/df_e$ in SABL for different vegetation types (Fig. 8b) are similar because of comparable Γ_θ. Most of the spread in the distribution is due to variability in heat storage or incoming solar radiation. Note that in Fig. 4 the regions that do not show a significant response due to lower range and variability in f_e are omitted. ERA5-derived $d(\Delta T_a)/df_e$ for forests is higher than the results from the SABL model. These higher values mainly correspond to tropical forests and can be connected to the variation in solar radiation due to clouds in those regions, which might alter ΔT_a and its response to f_e.

Next, we investigate the geographical variation of $d(\Delta T_a)/df_e$ observed in FLUXNET and modeled by SABL. Equation (5) indicates the dependency of $d(\Delta T_a)/df_e$ on solar radiation. Figure 8c shows the dependency of $d(\Delta T_a)/df_e$ to $R_{s,\max}$ observed in FLUXNET observations for the different vegetation types. These responses are sorted for different values of $R_{s,\max}$ (x axis) and the error bar represents the RMSE of these responses. We find that $d(\Delta T_a)/df_e$ increases (becomes more negative) with $R_{s,\max}$ by similar magnitudes across vegetation types. The linear regression of these responses (dashed line) shows that $d(\Delta T_a)/df_e$ increases (becomes more negative) by -6.5 K for an increase in $R_{s,\max}$ by 1000 W m^{-2}. We evaluate this sensitivity of ΔT_a to $R_{s,\max}$ in our SABL model (red area) by varying the value of Γ_θ between 4 and 10×10^{-3} K m^{-1}. We find that SABL produces a similar sensitivity as obtained using FLUXNET observations. Note that the daylight length is kept the same (12 h) in all cases for simplicity. The daylight length during summer is, however, longer, and increasingly so at higher latitudes, which introduces some bias into our results.

To conclude, our SABL model can reproduce global values of $d(\Delta T_a)/df_e$ similar to ERA5 and its sensitivity to solar radiation that is in agreement with FLUXNET observations.

The sensitivity analysis shows that the ΔT_a response to evaporative fraction is amplified in regions with high solar radiation, and this amplification is similar across vegetation types.

c. Explaining the ΔT_s response to evaporative fraction

We next use the SSEB model presented in section 2b to reproduce the response of ΔT_s to evaporative fraction. To do so, we use Eq. (9), which shows that $d(\Delta T_s)/df_e$ strongly depends on the aerodynamic conductance (g_a) and its diurnal amplitude (Δg_a). We derive these two quantities from the FLUXNET observations, and show the mean diurnal cycle of g_a for short vegetation, savanna, and forests in Fig. 9. Note that the mean aerodynamic conductance, g_a, is about twice as large for forests than for short vegetation. Additionally, g_a substantially increases during daytime, which is indicative of strong heat transfer from the surface to the atmosphere. The shaded region shows the standard deviation of g_a among vegetation types that is taken into account when formulating sensitivity of $d(\Delta T_s)/df_e$ to $R_{s,\max}$.

To estimate $d(\Delta T_s)/df_e$ across regions, we use $R_{s,\max}$ from ERA5 and $d(\Delta T_a)/df_e$ from observations. For g_a and Δg_a, we use the values shown in Fig. 9. Figure 10a shows the estimated response of ΔT_s to evaporative fraction. On comparing Figs. 10a and 8a we find that $d(\Delta T_s)/df_e$ is higher in magnitude and shows more geographical variability than $d(\Delta T_a)/df_e$, which is consistent with Figs. 4 and 5. Figure 10b shows the probability distributions of $d(\Delta T_s)/df_e$ from the SSEB model (red) and ERA5 for each vegetation type. In short vegetation, the SSEB model seems to reproduce the mean responses in ERA5. In savanna and forest, SSEB shows some slightly different distributions than ERA5, which might be simply because we used the observed mean of g_a and Δg_a. The consequence of using mean values of g_a from FLUXNET is evident in the biases in forests and savanna due to their high aerodynamic conductances and larger deviations from the mean (Fig. 9). In forests, the stronger responses of surface temperatures of the SSEB model are mainly because of the high values of $d(\Delta T_a)/df_e$ in ERA5, which is one of the inputs to the model (Fig. 8b).
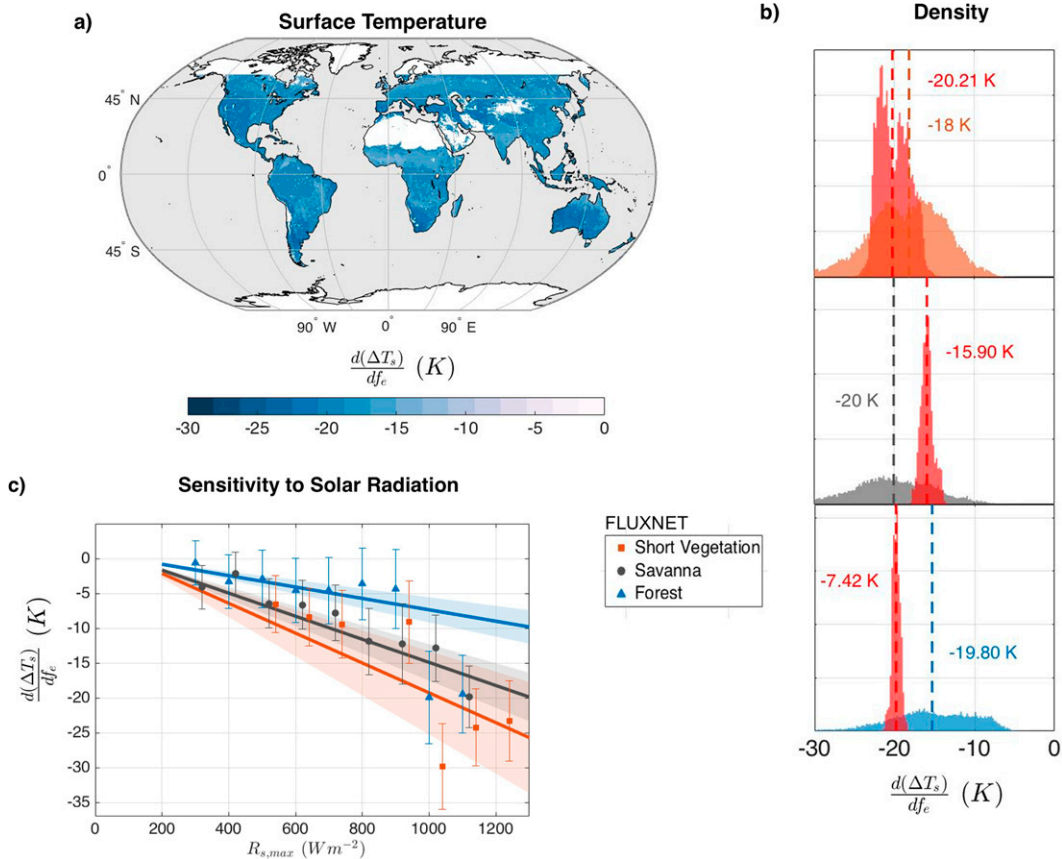
FIG. 10. The response of ΔT_s to evaporative fraction estimated from the SSEB model using values of g_a and Δg_a from FLUXNET and $R_{s,\max}$ from ERA5 in terms of (a) its mean geographic distribution, (b) its density distribution (red) compared to the one obtained from ERA5 for short vegetation, savanna, and forest (as shown in Fig. 4a), and (c) its sensitivity to maximum solar radiation, $R_{s,\max}$ (lines and shaded areas) compared to FLUXNET estimates (symbols) for short vegetation, savanna, and forests. The dashed lines in (b) indicate the median values of the distribution. The error bars in (c) represent the RMSE. The shaded area represents the standard error that mostly corresponds to g_a variations as shown in Fig. 9.

In addition to aerodynamic conductance, $d(\Delta T_s)/df_e$ is also sensitive to $R_{s,\max}$, which is visible in FLUXNET observations as shown in Fig. 10c. We find that the ΔT_s response to f_e increases in regions with stronger solar radiation, or greater $R_{s,\max}$. This sensitivity is larger for short vegetation than for forests. Our SSEB model also reproduces this sensitivity (shaded areas in Fig. 10c), matching the sensitivity from FLUXNET observations quite well. The shaded region shows the variation in these sensitivities due to the variation in g_a within each vegetation type.

Overall, the SSEB model captures most of the observed sensitivity of ΔT_s to f_e and $R_{s,\max}$. Our results emphasize the dominating role of aerodynamic conductance in cooling ΔT_s in forests. In contrast, in short vegetation, variations in f_e alter ΔT_s comparably to greater extent because of the lower aerodynamic conductance, and increasingly so in regions with greater solar radiation.

5. Discussion

In this work we evaluated ΔT_s and ΔT_a responses to evaporation in FLUXNET observations and ERA5 reanalyses. We found stronger responses of ΔT_s to evaporative fraction in short vegetation than in forests. Notably, the ΔT_a response to evaporative fraction is similar for short vegetation, savanna, and forests. ERA5 and FLUXNET-derived sensitivities show similar trends, being slightly stronger in ERA5. We demonstrate that this is due to systematic biases in ERA5's ΔT on dry (positive) and wet (negative) conditions, which also relates to the representation of surface energy components. The comparison of FLUXNET and ERA5's surface energy balance components show an overestimation of shortwave and net longwave radiative fluxes especially in short vegetation and forests. These biases are in agreement with the results shown by Urraca et al. (2018) and Jiang et al. (2020). Even though we used the finest spatial resolution of ERA5, these biases to some degree might represent blended information of the larger scale (31 km) in ERA5 and the MODIS IGBP vegetation classification than the local information provided by FLUXNET. Studies evaluating ERA5 products are currently limited (Martens et al. 2020; Bell et al. 2021; Simmons et al. 2021), and our study advocates investigating such biases

when employing ERA5's products in climate and hydrology research.

To explain the FLUXNET- and ERA5-based findings, we present two simple models that are based on fundamental physical concepts. Our SABL and SSEB models reproduce the local responses of ΔT_a and ΔT_s to evaporative fraction in ERA5 and their sensitivity to solar radiation in FLUXNET reasonably well.

The SABL model demonstrates that the change in boundary layer growth reduces the response of ΔT_a to evaporative fraction. Overall, the diurnal variation of air temperature is mainly constrained by the total solar radiation input into the boundary layer (reduced by the latent heat flux). This is in agreement with our previous interpretation (Panwar et al. 2019) where we showed that in absence of boundary layer growth, the diurnal amplitude of air temperature would be as large as the diurnal amplitude of surface temperature.

Our SABL model is rather simple because it only requires information on solar radiation and background lapse rate to estimate $d(\Delta T_a)/df_e$. Using ERA5 we show some variation in Γ_θ. For further understanding of PBL processes, it would be interesting to explore the factors shaping Γ_θ. Furthermore, it should be possible to obtain better estimates of the heat storage changes in the boundary layer by integrating the information of the vertical profile of temperature and humidity. Generally, studies to investigate the sensitivity of the boundary layer to soil moisture use more sophisticated boundary layer models and observations as shown by Santanello et al. (2011), Wouters et al. (2019), and Denissen et al. (2021). Such modeling approaches provide critical insights on controls of soil moisture in shaping boundary layer dynamics and air temperature (Dirmeyer and Brubaker 2007; Koster et al. 2011; Green et al. 2017; Gentine et al. 2019). What our results show is that the non-latent energy input into the boundary layer is the dominant factor that explains its dynamics, resulting in weaker responses of ΔT_a to f_e.

Our SSEB model shows that the ΔT_s response to evaporative fraction strongly depends on the aerodynamic conductance (which depends on vegetation type) and solar radiation. Our model assumes negligible effects of the ground heat flux and biomass heat storage (Gu et al. 2007; Lindroth et al. 2010; Swenson et al. 2019). Meier et al. (2019) showed that the heat stored in the forest biomass is relatively small (25–80 W m^{-2}) and dampens the diurnal temperature variation only by 1 K, which justifies our assumptions. Some variance in our model can likely to be further reduced by improving the calculation of aerodynamic conductance, that is currently based on the sensible heat flux. Additionally, to estimate the ΔT_s sensitivity we do not require information on the boundary layer that was otherwise integrated in earlier models (Diak 1990; Norman et al. 1995; Anderson et al. 1997; Kustas and Norman 1999). One might argue that the estimation of $d(\Delta T_s)/df_e$ requires $d(\Delta T_a)/df_e$ that depends on boundary layer dynamics. However, we also show that $d(\Delta T_a)/df_e$ has very small, comparatively uniform value that can be obtained from the solar energy input (reduced by the latent heat flux), so consequently, $d(\Delta T_s)/df_e$ does not need information on boundary layer dynamics. Therefore, it can be argued that surface

temperature is more strongly coupled to surface properties rather than boundary layer processes.

The SSEB model and data analysis shows that $d(\Delta T_s)/df_e$ is higher in short vegetation than in forests. The lower value of $d(\Delta T_s)/df_e$ in forests appears to contradict the known cooling effect of evaporation. Clearly, forests can maintain high evaporation via their deep root system (Kleidon and Heimann 2000), which maintains water availability in dry episodes. However, our SSEB model shows that in addition to evaporation, their high aerodynamic conductance is the primary cooling agent. In our model aerodynamic conductance represents vegetation effects at the ecosystem scale. To examine the leaf scale response and its impact on diurnal temperature variation, one could potentially look at the stomata–atmosphere coupling that is widely quantified by the decoupling factor (Jarvis and McNaughton 1986). In general, short vegetation is expected to be more strongly decoupled from the atmosphere than forests (Meinzer et al. 1993; Lee and Black 1993; Whitehead et al. 1984; Jarvis 1985), meaning that transpiration in short vegetation is mainly controlled by solar radiation and less by changes in stomatal conductance. However, previous studies have also shown high degree of variation in the decoupling factor for different ecosystems (Lin et al. 2015; Miner et al. 2017; Kauwe et al. 2017). Our study considers water limitation as the main control of evaporation, rather than stomatal conductance. Hence, further studies on stomatal controls on evaporative fraction and its relevance to global change could be beneficial.

Model sensitivities as well as FLUXNET observations show that $d(\Delta T)/df_e$ depends on solar radiation, indicating stronger impact of drought or dryness in regions with high solar radiation. For instance, in the tropics, ΔT_s of short vegetation is more sensitive to evaporation than in forests. Therefore, it can be anticipated that in the tropics, the increase in ΔT_s would be higher due to tropical deforestation than in the higher latitudes. This notion is in line with previous studies that show similar findings based on climate model simulations (Davin and de Noblet-Ducoudré 2010; Pitman et al. 2012; Lawrence et al. 2012; Li et al. 2018; Chen and Dirmeyer 2019b). We suggest that the lower response of temperature to deforestation-induced dryness in higher latitudes is mainly due to lower solar energy as also indicated by previous studies (Claussen et al. 2001; Brovkin et al. 2006; Mahmood et al. 2014; Longobardi et al. 2016).

Our findings are broadly consistent with previous studies. Surface temperature can be a good proxy for evaporative conditions (Su 2002; Kalma et al. 2008), but it also depends on vegetation type. The diurnal variation in surface temperature may be useful to quantify the impact of land use and land cover change, which has also been proposed by Li et al. (2015) and Bright et al. (2017). Similarly, Chen and Dirmeyer (2019a) show stronger daytime warming of surface temperature due to deforestation but discrepancies in air temperature due to differing turbulent characteristics. The distinction between surface and air temperature is also important because they are usually considered to be a proxy of each other, especially in developing temperature products (Zhang et al. 2011; Oyler et al. 2016). Similar observations were made by Mildrexler

et al. (2011), who looked at the relationship between remotely sensed land surface and in situ air temperatures data and interpreted this as the cooling effect of forests.

Finally, our simple models can be useful tools to analyze the different sensitivity of surface and air temperature trends to global changes, especially associated to drought and deforestation. The differences in surface and air temperature could be used to understand the different controls on land–atmosphere interactions. For instance, the diurnal variation of air temperature could be used to obtain the boundary layer height, and surface temperature to obtain aerodynamic conductance of vegetation. It would also be intriguing to evaluate how the compensating effect of boundary layer dynamics would adjust the response of the diurnal variation of air temperature in global warming scenarios. Which role could vegetation and altered water availability play in modulating the diurnal temperatures? So far, our study shows that it is mainly the solar energy input and not the vegetation type that controls the dynamics of the land–atmosphere system. Previous studies (Dai et al. 2006; Zhou et al. 2009; Lauritsen and Rogers 2012) show that the effect of clouds combined with soil moisture effect can reduce ΔT by 50%. Our approach can further be extended for cloudy versus clear-sky conditions to incorporate the radiative effects of clouds (see Fig. A4).

6. Summary and conclusions

Our study evaluated the response of ΔT_s and ΔT_a to changes in evaporative fraction in FLUXNET observations and ERA5 reanalyses and examined the underlying physical constraints that can explain these responses. We found that ΔT_s decreases strongly in response to changes in evaporative fraction, particularly in short vegetation. Contrarily, the ΔT_a response to evaporative fraction is weaker and similar across vegetation types. We also found that ERA5 appears to overestimate the sensitivity of the diurnal temperature range to evaporative fraction compared to FLUXNET.

We used two models based on physical constraints to explain these trends found in FLUXNET and ERA5. We found that ΔT_s is related to the surface energy partitioning and the aerodynamic conductance, which differs among vegetation types, whereas ΔT_a is primarily determined by the total, non-latent energy input into the lower atmosphere. Based on the surface energy balance we provide an expression for $d(\Delta T_s)/df_e$ that mainly depends on the aerodynamic conductance of vegetation and absorbed solar radiation. Similarly, $d(\Delta T_a)/df_e$ is obtained from a simple heat storage model of the lower atmosphere and it mainly depends on solar radiation and the background lapse rate of potential temperature. Our simple models also capture the observed sensitivity of $d(\Delta T_s)/df_e$ and $d(\Delta T_a)/df_e$ to solar radiation that can explain the geographical variation of these responses.

Since our energy balance-based models are able to reproduce the identified responses in FLUXNET and ERA5 datasets, we can draw the following conclusions. The main patterns of diurnal temperature ranges mainly reflect how solar radiation is being partitioned at the surface, and how the non-latent energy components are then buffered in the lower atmosphere.
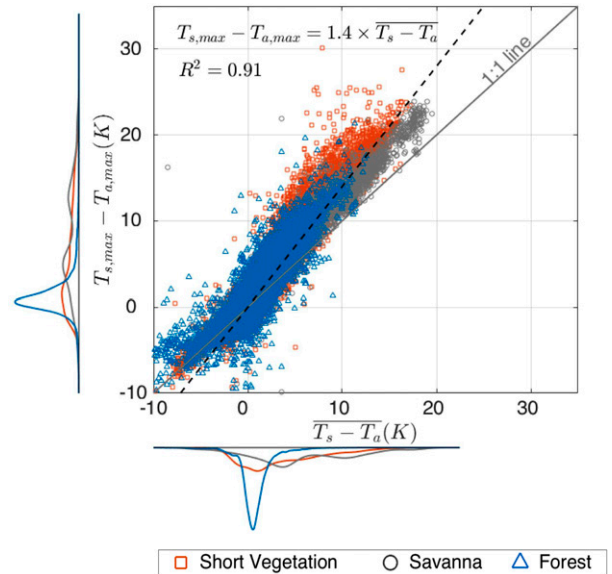

FIG. A1. The relationship between $T_{s,max} - T_{a,max}$ and $\overline{T_s - T_a}$ in FLUXNET sites of short vegetation, savanna, and forests. Each data point shows the value for one day at a site during the time period considered. The dotted line represents the linear regression of the relationship between $T_{s,max} - T_{a,max}$ and $\overline{T_s - T_a}$.

Both aspects reflect the constraints imposed by the energy balances of the surface and of the lower atmosphere. What this implies is that the main coupling between the land surface and the atmosphere is represented by the strongly constrained response of the convective boundary layer to surface heating, as it is the dominant buffer that levels out the strong variation of solar radiation during the diurnal cycle.

Our findings suggests that surface temperature is a robust metric for evaporative conditions and vegetation properties, whereas air temperature provides unique information on boundary layer dynamics and heat storage changes. The different physical constraints of surface and air temperature shall be considered when using them as proxies of each other. Our results imply that surface temperature is better suited to detect impacts of deforestation than the more commonly used air temperature.

To summarize, our findings clearly show that land–atmosphere processes shape the diurnal variation of surface and air temperature differently. This distinction between diurnal surface and air temperature is important when analyzing trends in climate science. Our study can be used for further exploring the process-based sensitivities of diurnal surface and air temperatures to land cover change and global climate change.

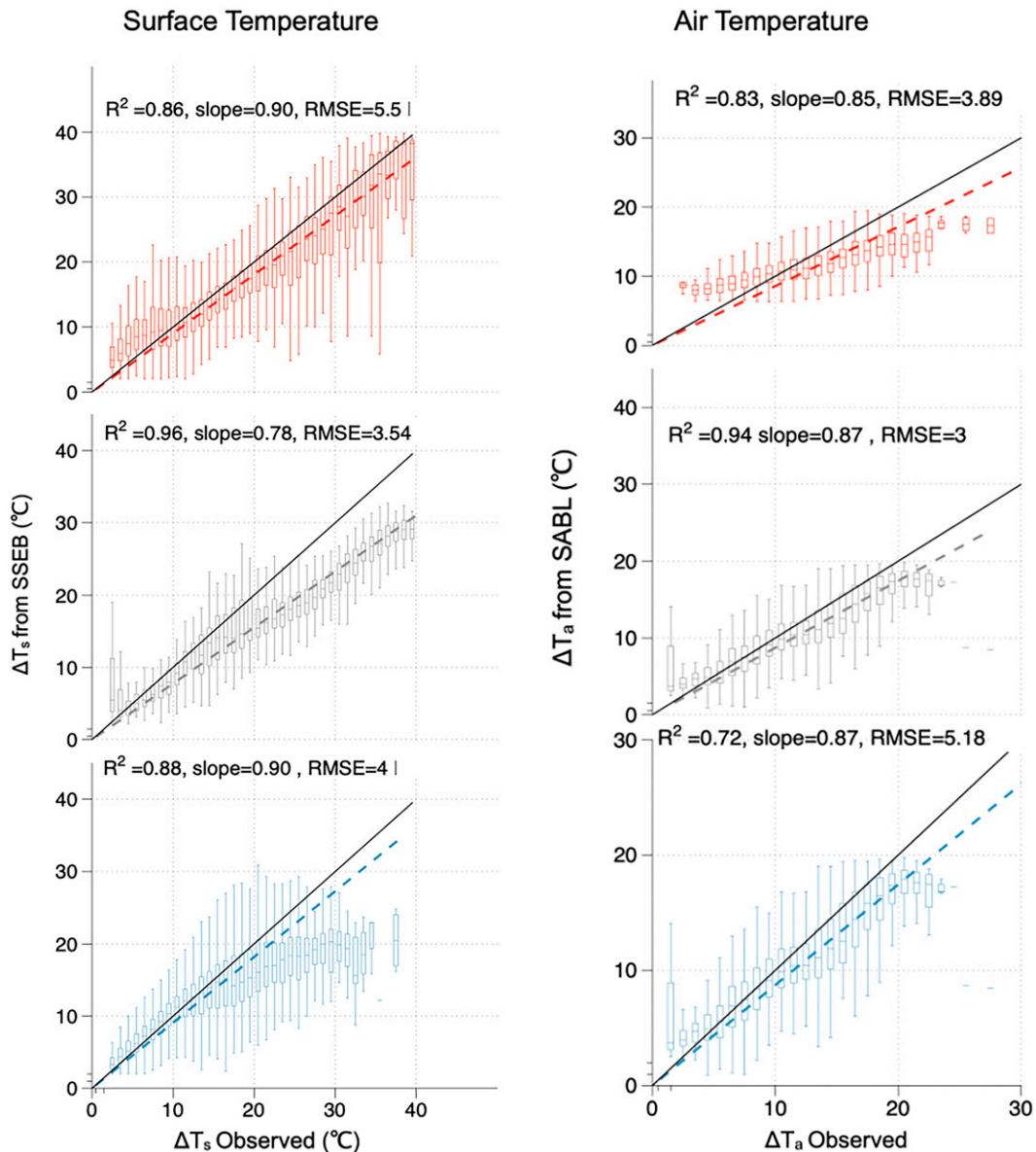FIG. A2. Comparison of diurnal surface (ΔT_s) and air (ΔT_a) temperature range obtained from the SSEB and SABL models (y axis), respectively, to the observed values at FLUXNET (x axis) for short vegetation (red), savanna (gray), and forests (blue). The correlation coefficient (R^2), the slope of the linear regression, and root-mean-square values (RMSE) are provided for the corresponding plots.

use R and Matlab programming languages for analysis and plotting.

Data availability statement. The FLUXNET data are available at https://FLUXNET.fluxdata.org/; all of the FLUXNET data cited herein were downloaded on 23 October 2020. More descriptions of each FLUXNET site (160 sites) used in this study are provided in appendix A. The ERA5 reanalysis data are available on the Copernicus Climate Change Service (C3S) Climate Data Store at https://cds.climate.copernicus.eu/

doi/10.24381/cds.e2161bac. The IGBP land cover class used for vegetation classification for FLUXNET sites is available at https://doi.org/10.3334/ORNLDAAC/1530.

APPENDIX A

Appendix Figures and Tables

Figure A1 shows the relationship between the differences in mean (x axis) and maximum (y axis) temperatures between the
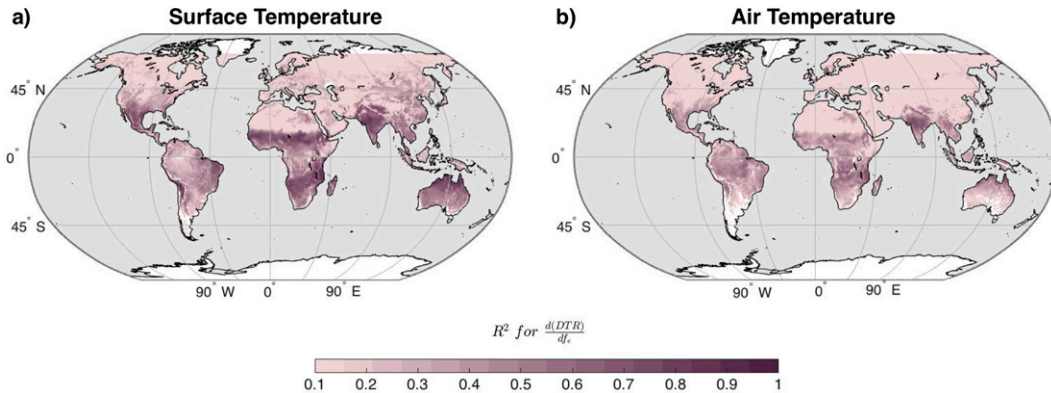
FIG. A3. The correlation coefficient (R^2) for the local responses of ΔT_s and ΔT_a to evaporative fraction in ERA5. The local responses are obtained from the linear regression of daily values of DTR and f_e.

surface and at 2-m height. Each point represents the daily values obtained at FLUXNET sites of short vegetation, savanna, and forests. The dashed line represents the linear regression of their relationship. We found that the differences of their maximum is about 1.4 times the differences of their mean values across vegetation types. This relationship is used to simplify Eq. (7) into Eq. (8).

Figure A2 shows the comparison of the observed diurnal range of surface and air temperature (x axis) with the one estimated using the SSEB and SABL models (y axis). The observations and input to the models are obtained from FLUXNET sites of short vegetation (red), savanna (gray) and forests (blue).

The SABL and SSEB models predict the diurnal variation of temperatures quite well with high correlation coefficient. The slopes of the estimates are lower than one, meaning the diurnal variations predicted by the models are lower than the observed one, especially for warmer and/or high solar radiation conditions. This is likely due to the simplifications of physical processes in SABL and SSEB models that have been discussed in detail in the methods and discussion sections. It should be noted that our models are mainly developed to obtain temperatures sensitivities to evaporation and therefore they include some assumptions that may lead to biases when using them to estimate diurnal range of temperature.

Figure A3 shows the correlation coefficient of local responses of the diurnal temperature ranges to changes in evaporative conditions. These responses are calculated using daily data from the ERA5 reanalysis for years 2000–15. High R^2 values indicate stronger responses of diurnal temperature ranges to changes in evaporative fractions. Not all regions have high R^2. Lower R^2 values can be linked to limited variations of evaporative fraction in the grid cell, for instance in deserts due to limited water or at high latitudes due to limited energy input. Only a few regions have high R^2 that are also shown in Figs. 4a and 4b.

Table A1 provides the description of each FLUXNET site used in the study, and Table A2 describes the variables used from FLUXNET observations and ERA5 reanalyses.

Figure A4 evaluates the effect of clouds on our results. It shows that under cloudy conditions, solar radiation is reduced, which lowers the sensitivities of the diurnal temperature ranges to evaporative fraction. These values are obtained for short vegetation FLUXNET sites. Cloudy days are here taken as days when the observed solar radiation is less than 30% of the potential solar radiation. It is observed that the diurnal range of surface temperature reduces by 15 K on cloudy days but only by 3 K for the diurnal range of air temperature.

Cloud effects on diurnal temperature ranges can also be estimated by the SABL and SSEB models. Based on Eq. (5), $d(\Delta T_a)/df_e$ for cloudy conditions ($R_s = 100$ W m^{-2}) is only -2.8 K, and for noncloudy conditions ($R_s = 220$ W m^{-2}) it is -4.2 K. Similarly, based on Eq. (9), the sensitivity of the diurnal range of surface temperature $[d(\Delta T_s)/df_e]$ for noncloudy conditions ($R_s = 220$ W m^{-2}) is -17 K whereas for cloudy conditions ($R_s = 100$ W m^{-2}) it is -8 K. These values are similar to the values obtained from observations (Fig. A4).

APPENDIX B

Derivation of ΔU

We derive an expression for the diurnal heat storage change ΔU in the boundary layer using the energy balance constraint as described in (Kleidon and Renner 2017). We seek the input of nonlatent energy into the lower atmosphere, so we need to subtract the latent heat flux, LE, from the solar energy input by absorption at the surface, R_s. We use the maximum power limit of the cold heat engine (Kleidon and Renner 2018) to get an expression of the turbulent heat fluxes, and then use the evaporative fraction f_e to infer LE.

The optimum heat flux from maximum power is given by

$$J_{\text{opt}} = \frac{1}{2}\left(R_s + \frac{dU}{dt}\right), \tag{B1}$$

where R_s is absorbed solar radiation at the surface and dU/dt is the heat storage variation in the boundary layer (assuming

TABLE A1. Description of FLUXNET sites used in this study.

Site No.	IGBP Land use	Site ID	Site name	Location Lat (°)	Location Lon (°)	Data citation
1	Open shrublands	AU-ASM	Alice Springs	−22.28	133.25	Cleverly and Eamus (2016a)
2	Closed shrublands	AU-Cpr	Calperum	−34.00	140.59	Meyer et al. (2016)
3	Croplands	AU-Rig	Riggs Creek	−36.66	145.58	Beringer et al. (2016a)
4	Grasslands	AU-Stp	Sturt Plains	−17.15	133.35	Beringer and Hutley (2016f)
5	Open shrublands	AU-TTE	Ti Tree East	−22.29	133.64	Cleverly and Eamus (2016b)
6	Croplands	AU-Ync	Australia Yanco site	−34.99	146.29	Beringer and Walker (2016)
7	Croplands	BE-Lon	Lonzee	50.55	4.75	De Ligne et al. (2016b)
8	Croplands	CA-TP1	ON-Turkey Point 2002 White Pine	42.66	−80.56	Arain (2016a)
9	Croplands	CA-TP2	ON-Turkey Point 1989 White Pine	42.77	−80.46	Arain (2016b)
10	Croplands	CH-Cha	Chamau grassland	47.21	8.41	Merbold et al. (2020)
11	Croplands	CH-Fru	Fruebuel grassland	47.12	8.54	Hörtnagl et al. (2016c)
12	Croplands	CH-Oe1	Oensingen1 grass	47.29	7.73	Ammann (2016)
13	Croplands	CH-Oe2	Oensingen2 crop	47.29	7.73	Hörtnagl et al. (2016d)
14	Grasslands	CN-Dan	Damxung	30.85	91.08	Shi et al. (2016)
15	Grasslands	CN-Du2	Duolun-grassland	42.05	116.28	Chen (2016)
16	Grasslands	CN-Ha2	Haibei Shrubland	37.67	101.33	Li (2016)
17	Croplands	CZ-wet	CZECHWET	49.02	14.77	Dusek et al. (2016)
18	Croplands	DE-Geb	Gebesee	51.10	10.91	Brümmer et al. (2016)
19	Croplands	DE-Kli	Klingenberg	50.89	13.52	Bernhofer et al. (2016b)
20	Grasslands	DE-RuR	Rollesbroich	50.62	6.30	Schmidt and Graf (2016)
21	Croplands	DE-Seh	Selhausen	50.87	6.45	Schneider and Schmidt (2016)
22	Croplands	DE-Zrk	Zarnekow	53.88	12.89	Sachs et al. (2016)
23	Croplands	DK-Eng	Enghave	55.69	12.19	Pilegaard and Ibrom (2016)
24	Croplands	DK-Fou	Foulum	56.48	9.59	Olesen (2016)
25	Closed shrublands	ES-Amo	Amoladeras	36.83	−2.25	Poveda et al. (2016)
26	Closed shrublands	ES-LJu	Llano de los Juanes	36.93	−2.75	Cañete et al. (2016)
27	Croplands	FR-Gri	Grignon	48.84	1.95	Buysse et al. (2016)
28	Croplands	FR-LBr	Le Bray (after 28 Jun 1998)	44.72	−0.77	Berbigier and Loustau (2016)
29	Croplands	IT-BCi	Borgo Cioffi	40.52	14.96	Magliulo et al. (2016)
30	Croplands	IT-CA1	Castel d'Asso1	42.38	12.03	Sabbatini et al. (2016c)
31	Croplands	IT-CA2	Castel d'Asso2	42.38	12.03	Sabbatini et al. (2016a)
32	Croplands	IT-CA3	Castel d'Asso 3	42.38	12.02	Sabbatini et al. (2016b)
33	Grasslands	IT-MBo	Monte Bondone	46.01	11.05	Gianelle et al. (2016a)
34	Croplands	IT-PT1	Zerbolo-Parco Ticino-Canarazzo	45.20	9.06	Manca and Goded (2016)
35	Croplands	IT-Ro1	Roccarespam pani1	42.41	11.93	Valentini et al. (2016c)
36	Croplands	IT-Ro2	Roccarespam pani2	42.39	11.92	Papale et al. (2016)
37	Croplands	JP-SMF	Seto Mixed Forest Site	35.25	137.07	Kotani (2016b)
38	Croplands	PA-SPn	Sardinilla Plantation	9.32	−79.63	Wolf et al. (2016a)
39	Croplands	PA-SPs	Sardinilla Pasture	9.31	−79.63	Wolf et al. (2016b)
40	Grasslands	RU-Ha1	Ubs Nur-Hakasija–grassland	54.73	90.00	Belelli et al. (2016)
41	Grasslands	SD-Dem	Demokeya	13.28	30.48	Ardö et al. (2016)
42	Grasslands	SN-Dhr	Dahra	15.40	−15.43	Tagesson et al. (2016)
43	Grasslands	U.S.-AR1	ARM USDA UNL OSU Woodward Switchgrass 1	36.43	−99.42	Billesbach et al. (2016a)
44	Grasslands	U.S.-AR2	ARM USDA UNL OSU Woodward Switchgrass 2	36.64	−99.60	Billesbach et al. (2016b)
45	Croplands	U.S.-ARM	ARM Southern Great Plains site	36.61	−97.49	Biraud et al. (2016)
46	Croplands	U.S.-ARb	ARM Southern Great Plains burn site	35.55	−98.04	Torn (2016a)
47	Grasslands	U.S.-ARc	ARM Southern Great Plains control site	35.55	−98.04	Torn (2016b)
48	Grasslands	U.S.-Cop	Corral Pocket	38.09	−109.39	Bowling (2016)
49	Croplands	U.S.-Goo	Goodwin Creek	34.25	−89.87	Meyers (2016a)
50	Croplands	U.S.-IB2	Fermi National Accelerator Laboratory	41.84	−88.24	Matamala (2016)

TABLE A1. (*Continued*)

Site No.	IGBP Land use	Site ID	Site name	Lat (°)	Lon (°)	Data citation
				Location		
51	Grasslands	U.S.-LWW	Little Washita Watershed	34.96	−97.98	Meyers (2016b)
52	Croplands	U.S.-Me1	Metolius Eyerly Burn	44.58	−121.50	Law (2016a)
53	Croplands	U.S.-Ne1	Mead–irrigated continuous maize site	41.17	−96.48	Suyker (2016a)
54	Croplands	U.S.-Ne2	Mead–irrigated maize-soybean rotation site	41.16	−96.47	Suyker (2016b)
55	Croplands	U.S.-Ne3	Mead–rainfed maize-soybean rotation site	41.18	−96.44	Suyker (2016c)
56	Open shrublands	U.S.-SRC	Santa Rita Creosote	31.91	−110.84	Kurc (2016)
57	Grasslands	U.S.-SRG	Santa Rita Grassland	31.79	−110.83	Scott (2016a)
58	Open shrublands	U.S.-SRM	Santa Rita Mesquite	31.82	−110.87	Scott (2016b)
59	Open shrublands	U.S.-Sta	Saratoga	41.40	−106.80	Ewers and Pendall (2016)
60	Croplands	U.S.-Twt	Twitchell Island	38.11	−121.65	Baldocchi (2016)
61	Open shrublands	U.S.-Whs	Walnut Gulch Lucky Hills Shrubland	31.74	−110.05	Scott (2016c)
62	Croplands	U.S.-Wi6	Pine barrens 1 (PB1)	46.62	−91.30	Chen (2016c)
63	Grasslands	U.S.-Wkg	Walnut Gulch Kendall Grasslands	31.74	−109.94	Scott (2016d)
64	Savannas	AU-Ade	Adelaide River	−13.08	131.12	Beringer and Hutley (2016a)
65	Woody Savannas	AU-Cum	Cumberland Plains	−33.61	150.72	Pendall and Griebel (2016)
66	Savannas	AU-DaP	Daly River Pasture	−14.06	131.32	Beringer and Hutley (2016b)
67	Savannas	AU-DaS	Daly River Savanna	−14.16	131.39	Beringer and Hutley (2016g)
68	Savannas	AU-Dry	Dry River	−15.26	132.37	Beringer and Hutley (2016c)
69	Savannas	AU-Fog	Fogg Dam	−12.55	131.31	Beringer and Hutley (2016d)
70	Woody savannas	AU-Gin	Gingin	−31.38	115.65	Macfarlane et al. (2016)
71	Savannas	AU-How	Howard Springs	−12.5	131.15	Beringer and Hutley (2016e)
72	Woody savannas	AU-Whr	Whroo	−36.67	145.03	Beringer et al. (2016b)
73	Woody savannas	CG-Tch	Tchizalamou	−4.29	11.66	Nouvellon (2016)
74	Woody savannas	CN-Qia	Qianyanzhou	26.73	115.07	Wang and Fu (2016)
75	Woody savannas	ES-LgS	Laguna Seca	37.1	−2.97	Reverter et al. (2016)
76	Woody savannas	IT-Isp	Ispra ABC-IS	45.81	8.63	Gruening et al. (2016a)
77	Woody savannas	IT-Noe	Sardinia/Arca di Noe	40.61	8.15	Spano et al. (2016)
78	Woody savannas	U.S.-KS2	Kennedy Space Center (scrub oak)	28.61	−80.67	Drake and Hinkle (2016b)
79	Woody savannas	U.S.-Me6	Metolius New Young Pine	44.32	−121.6	Law (2016f)
80	Woody savannas	U.S.-Myb	Mayberry Wetland	38.05	−121.77	Sturtevant et al. (2016)
81	Woody savannas	U.S.-Ton	Tonzi Ranch	38.43	−120.97	Baldocchi and Ma (2016)
82	Woody savannas	U.S.-Var	Vaira Ranch	38.41	−120.95	Baldocchi et al. (2016)
83	Savannas	ZM-Mon	Mongo	−15.44	23.25	Kutsch et al. (2016)
84	Mixed forests	AT-Neu	Neustift/Stubai Valley	47.12	11.32	Wohlfahrt et al. (2016)
85	Evergreen broadleaf forest	AU-Tum	Tumbarumba	−35.66	148.15	Woodgate et al. (2016)
86	Evergreen broadleaf forest	AU-Wac	Wallaby Creek	−37.43	145.19	Beringer et al. (2016c)
87	Evergreen broadleaf forest	AU-Wom	Wombat	−37.42	144.09	Arndt et al. (2016)
88	Mixed forests	BE-Bra	Brasschaat (De Inslag Forest)	51.31	4.52	Neirynck et al. (2016)
89	Mixed forests	BE-Vie	Vielsalm	50.31	6.00	De Ligne et al. (2016a)
90	Evergreen broadleaf forest	BR-Sa1	Santarem-Km67-Primary Forest	−2.86	−54.96	Saleska (2016)
91	Evergreen broadleaf forest	BR-Sa3	Santarem-Km83-Logged Forest	−3.02	−54.97	Goulden (2016a)
92	Mixed forests	CA-Gro	ON-Groundhog River Mixedwood	48.22	−82.16	McCaughey (2016)
93	Evergreen needleleaf forest	CA-Man	MB-Northern Old Black Spruce	55.88	−98.48	Amiro (2016a)
94	Evergreen needleleaf forest	CA-NS1	UCI 1850	55.88	−98.48	Goulden (2016b)
95	Evergreen needleleaf forest	CA-NS2	UCI 1930	55.91	−98.52	Goulden (2016c)
96	Evergreen needleleaf forest	CA-NS3	UCI 1964	55.91	−98.38	Goulden (2016d)
97	Evergreen needleleaf forest	CA-NS4	UCI 1964 wet	55.91	−98.38	Goulden (2016e)
98	Evergreen needleleaf forest	CA-NS5	UCI 1981	55.86	−98.49	Goulden (2016f)

TABLE A1. (*Continued*)

Site No.	IGBP Land use	Site ID	Site name	Location Lat (°)	Location Lon (°)	Data citation
99	Evergreen needleleaf forest	CA-NS6	UCI 1989	55.92	−98.96	Goulden (2016g)
100	Evergreen needleleaf forest	CA-NS7	UCI 1998	56.64	−99.95	Goulden (2016h)
101	Mixed forests	CA-Oas	SK-Old Aspen	53.63	−106.20	Black (2016a)
102	Evergreen needleleaf forest	CA-Obs	SK-Southern Old Black Spruce	53.99	−105.12	Black (2016b)
103	Evergreen needleleaf forest	CA-Qfo	QC-Eastern Old Black Spruce (EOBS)	49.69	−74.34	Margolis (2016)
104	Evergreen needleleaf forest	CA-SF1	SK-1977 Fire	54.48	−105.82	Amiro (2016b)
105	Mixed forests	CA-SF2	SK-1989 Fire	54.25	−105.88	Amiro (2016c)
106	Evergreen needleleaf forest	CA-SF3	SK-1998 Fire	54.09	−106.01	Amiro (2016d)
107	Mixed forests	CA-TP3	ON-Turkey Point 1974 White Pine	42.71	−80.35	Arain (2016c)
108	Deciduous broadleaf forest	CA-TPD	ON-Turkey Point Deciduous	42.64	−80.56	Arain (2016d)
109	Evergreen needleleaf forest	CH-Dav	Davos–Seehorn forest	46.82	9.86	Hörtnagl et al. (2016b)
110	Mixed forests	CH-Lae	Laegeren	47.48	8.37	Hörtnagl et al. (2016a)
111	Mixed forests	CN-Cha	Changbaishan	42.40	128.10	Zhang and Han (2016)
112	Evergreen broadleaf forest	CN-Din	Dinghushan	23.17	112.53	Zhou and Yan (2016)
113	Mixed forests	CZ-BK2	Bily Kriz-grassland	49.49	18.54	Sigut et al. (2016)
114	Mixed forests	DE-Gri	Grillenburg-grass station	50.95	13.51	Bernhofer et al. (2016a)
115	Mixed forests	DE-Hai	Hainich	51.08	10.45	Knohl et al. (2016b)
116	Evergreen needleleaf forest	DE-Lkb	Lackenberg	49.10	13.30	Lindauer et al. (2016)
117	Deciduous broadleaf forest	DE-Lnf	Leinefelde	51.33	10.37	Knohl et al. (2016a)
118	Evergreen needleleaf forest	DE-Obe	Oberbarenburg	50.78	13.72	Bernhofer et al. (2016c)
119	Evergreen needleleaf forest	DE-SfN	Schechenfilz Nord	47.81	11.33	Klatt et al. (2016)
120	Mixed forests	DE-Spw	Spreewald	51.89	14.03	Bernhofer et al. (2016d)
121	Evergreen needleleaf forest	DE-Tha	Tharandt-Anchor Station	50.96	13.57	Bernhofer et al. (2016e)
122	Deciduous broadleaf forest	DK-Sor	Soroe-LilleBogeskov	55.49	11.64	Ibrom and Pilegaard (2016)
123	Deciduous broadleaf forest	FR-Fon	Fontainebleau	48.48	2.78	Berveiller et al. (2016)
124	Mixed forests	FR-Pue	Puechabon	43.74	3.60	Ourcival (2016)
125	Evergreen broadleaf forest	GF-Guy	Guyaflux	5.28	−52.92	Bonal and Burban (2016)
126	Evergreen broadleaf forest	GH-Ank	Ankasa	5.27	−2.69	Valentini et al. (2016b)
127	Deciduous broadleaf forest	IT-Col	Collelongo-Selva Piana	41.85	13.59	Matteucci (2016)
128	Evergreen needleleaf forest	IT-Cp2	Castelporziano2	41.70	12.36	Fares et al. (2016)
129	Evergreen needleleaf forest	IT-Cpz	Castelporziano	41.71	12.38	Valentini et al. (2016a)
130	Evergreen needleleaf forest	IT-La2	Lavarone2	45.95	11.29	Cescatti et al. (2016)
131	Evergreen needleleaf forest	IT-Lav	Lavarone (after March 2002)	45.96	11.28	Gianelle et al. (2016b)
132	Evergreen needleleaf forest	IT-Ren	Renon/Ritten (Bolzano)	46.59	11.43	Montagnani and Minerbi (2016)
133	Mixed forests	IT-SR2	San Rossore 2	43.73	10.29	Gruening et al. (2016b)
134	Evergreen needleleaf forest	IT-Tor	Torgnon	45.84	7.58	Cremonese et al. (2016)
135	Mixed forests	JP-MBF	Moshiri Birch Forest Site	44.38	142.32	Kotani (2016a)
136	Evergreen broadleaf forest	MY-PSO	Pasoh Forest Reserve	2.97	102.31	Kosugi and Takanashi (2016)
137	Mixed forests	NL-Hor	Horstermeer	52.24	5.07	Dolman et al. (2016)
138	Evergreen needleleaf forest	NL-Loo	Loobos	52.17	5.74	Moors and Elbers (2016)
139	Mixed forests	RU-Fyo	Fedorovskoje-drained spruce stand	56.46	32.92	Varlagin et al. (2016)
140	Evergreen needleleaf forest	U.S.-Blo	Blodgett Forest	38.90	−120.63	Goldstein (2016)
141	Evergreen needleleaf forest	U.S.-GBT	GLEES Brooklyn Tower	41.37	−106.24	Massman (2016a)
142	Evergreen needleleaf forest	U.S.-GLE	GLEES	41.36	−106.24	Massman (2016b)
143	Mixed forests	U.S.-Ha1	Harvard Forest EMS Tower (HFR1)	42.54	−72.17	Munger (2016)
144	Mixed forests	U.S.-KS1	Kennedy Space Center (slash pine)	28.46	−80.67	Drake and Hinkle (2016a)
145	Mixed forests	U.S.-Los	Lost Creek	46.08	−89.98	Desai (2016a)
146	Deciduous broadleaf forest	U.S.-MMS	Morgan Monroe State Forest	39.32	−86.41	Novick and Phillips (2016)
147	Evergreen needleleaf forest	U.S.-Me2	Metolius Intermediate Pine	44.45	−121.56	Law (2016b)
148	Evergreen needleleaf forest	U.S.-Me3	Metolius Second Young Pine	44.32	−121.61	Law (2016c)
149	Evergreen needleleaf forest	U.S.-Me4	Metolius Old Pine	44.50	−121.62	Law (2016d)

TABLE A1. (*Continued*)

Site No.	IGBP Land use	Site ID	Site name	Lat (°)	Lon (°)	Data citation
				Location		
150	Evergreen needleleaf forest	U.S.-Me5	Metolius First Young Pine	44.44	−121.57	Law (2016e)
151	Evergreen needleleaf forest	U.S.-NR1	Niwot Ridge (LTER NWT1)	40.03	−105.55	Blanken et al. (2016)
152	Deciduous broadleaf forest	U.S.-Oho	Oak Openings	41.55	−83.84	Chen et al. (2016)
153	Mixed forests	U.S.-PFa	Park Falls	45.95	−90.27	Desai (2016b)
154	Mixed forests	U.S.-Syv	Sylvania Wilderness Area	46.24	−89.35	Desai (2016c)
155	Deciduous broadleaf forest	U.S.-UMB	Univ. of Mich. Biological Station	45.56	−84.71	Gough et al. (2016a)
156	Mixed forests	U.S.-UMd	Univ. of Mich. Biological Station Disturbance	45.56	−84.70	Gough et al. (2016b)
157	Deciduous broadleaf forest	U.S.-WCr	Willow Creek	45.81	−90.08	Desai (2016d)
158	Deciduous broadleaf forest	U.S.-Wi3	Mature hardwood (MHW)	46.63	−91.10	Chen (2016a)
159	Mixed forests	U.S.-Wi4	Mature red pine (MRP)	46.74	−91.17	Chen (2016b)
160	Mixed forests	U.S.-Wi9	Young Jack pine (YJP)	46.62	−91.08	Chen (2016d)

that the heat storage change in the soil is negligible). The heat storage increase during the day is given by

$$\frac{dU}{dt} = R_s - \mathrm{LE} = R_s - f_e J_{\mathrm{opt}}. \quad \text{(B2)}$$

When Eqs. (B1) and (B2) are combined, we obtain

$$\frac{dU}{dt} = \frac{2 - f_e}{2 + f_e} R_s. \quad \text{(B3)}$$

TABLE A2. Description of data used.

Variable name	Unit	Data source	Description	Spatial	Temporal
				Resolution	
Surface temperature (T_s)	K	FLUXNET	Calculated from the upwelling flux of longwave radiation emitted by the surface (Stefan–Boltzmann law)	Site level	Half hourly
		ERA5	Temperature of the uppermost surface layer, which has no heat capacity. Available as skin temperature (Copernicus Climate Change Service 2019)	0.25° lat–lon grid	Hourly
Air temperature (T_a)	K	FLUXNET	Usually measured 2 m above the canopy. For more details please refer to the site descriptions.	Site level	Half hourly
		ERA5	Air temperature 2 m above the surface calculated by interpolating between the lowest model level and Earth's surface (Copernicus Climate Change Service 2019)	0.25° lat–lon grid	Hourly
Evaporative fraction (f_e)	—	FLUXNET	The slope of the linear regression between the half hourly observations of latent heat flux (LE) and total turbulent heat flux (LE + H)	Site level	Half hourly
		ERA5		0.25° lat–lon grid	Hourly
Aerodynamic conductance (g_a)	m s^{-1}	FLUXNET	From the sensible heat flux, $g_a = H/[c_p\rho(T_s - T_a)]$	Site level	—
Vegetation type	—	IGBP-MODIS	Vegetation is classified into short vegetation (croplands, grasslands, and shrublands), savanna, and forests (decidous broadleaf, evergreen broadleaf, evergreen needleleaf, and mixed forests). For details on individual sites see Table A1 and Falge et al. (2017b)	Site level and 0.25° lat–lon grid	—

Solar Radiation

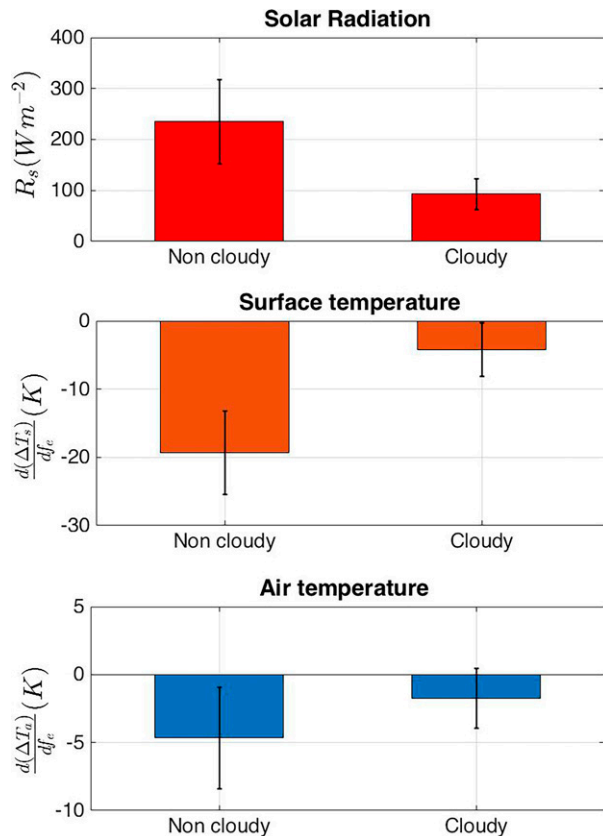
Surface temperature

Air temperature

FIG. A4. The impact of clouds on solar radiation and on the sensitivities of the diurnal temperature ranges to evaporative fraction. These relations are obtained from the FLUXNET observations for short vegetation sites.

Integrated over the daytime of solar energy input, this yields a magnitude of heat storage change, ΔU, in the lower atmosphere of

$$\Delta U = \frac{2 - f_e}{2 + f_e}\Delta U_0, \tag{B4}$$

where the heat storage variation in the absence of evaporation is given by the total absorbed solar energy during the day, $\Delta U_0 = R_{s,avg}\Delta t = (2/\pi)R_{s,max}\Delta t_{day}$ with Δt being 24 h, Δt_{day} being the daytime length, and $R_{s,max}$ being the maximum in solar absorption at the surface during the day at solar noon.

REFERENCES

Amiro, B., 2016a: FLUXNET2015 CA-Man Manitoba - Northern old black spruce (former BOREAS northern study area). FluxNet, University of Manitoba, https://www.osti.gov/dataexplorer/biblio/dataset/1440035.

——, 2016b: FLUXNET2015 CA-SF1 Saskatchewan - Western Boreal, forest burned in 1977. FluxNet, University of Manitoba, https://www.osti.gov/servlets/purl/1440046.

——, 2016c: FLUXNET2015 CA-SF2 Saskatchewan - Western Boreal, forest burned in 1989. FluxNet, University of Manitoba, https://www.osti.gov/servlets/purl/1440047.

——, 2016d: FLUXNET2015 CA-SF3 Saskatchewan - Western Boreal, forest burned in 1998. FluxNet, University of Manitoba; Canadian Forest Service, https://www.osti.gov/servlets/purl/1440048.

Ammann, C., 2016: FLUXNET2015 CH-Oe1 Oensingen Grassland. FluxNet, Agroscope Zuerich, https://www.osti.gov/servlets/purl/1440135.

Anderson, M., J. Norman, G. Diak, W. Kustas, and J. Mecikalski, 1997: A two-source time-integrated model for estimating surface fluxes using thermal infrared remote sensing. Remote Sens. Environ., 60, 195–216, https://doi.org/10.1016/S0034-4257(96)00215-5.

Arain, M. A., 2016a: FLUXNET2015 CA-TP1 Ontario - Turkey point 2002 plantation white pine. FluxNet, McMaster University, https://www.osti.gov/servlets/purl/1440050.

——, 2016b: FLUXNET2015 CA-TP2 Ontario - Turkey point 1989 plantation white pine. FluxNet, McMaster University, https://www.osti.gov/servlets/purl/1440051.

——, 2016c: FLUXNET2015 CA-TP3 Ontario - Turkey point 1974 plantation white pine. FluxNet, McMaster University, https://www.osti.gov/servlets/purl/1440052.

——, 2016d: FLUXNET2015 CA-TPD Ontario - Turkey point mature deciduous. FluxNet, McMaster University, https://www.osti.gov/servlets/purl/1440112.

Ardö, J., B. Tahir, and H. ElKhidir, 2016: FLUXNET2015 SD-Dem Demokeya. FluxNet, Lund University, https://www.osti.gov/servlets/purl/1440186.

Arndt, S., N. Hinko-Najera, A. Griebel, J. Beringer, and S. Livesley 2016: FLUXNET2015 AU-Wom Wombat. FluxNet, University of Melbourne, https://www.osti.gov/servlets/purl/1440207.

Baldocchi, D., 2016: FLUXNET2015 US-Twt Twitchell Island. FluxNet, University of California, Berkeley, https://www.osti.gov/servlets/purl/1440106.

——, and S. Ma, 2013: How will land use affect air temperature in the surface boundary layer? Lessons learned from a comparative study on the energy balance of an oak savanna and annual grassland in California, USA. Tellus, 65B, 19994, https://doi.org/10.3402/tellusb.v65i0.19994.

——, and ——, 2016: FLUXNET2015 US-Ton Tonzi Ranch. FluxNet, University of California, Berkeley, https://www.osti.gov/servlets/purl/1440092.

——, ——, and L. Xu, 2016: FLUXNET2015 US-Var Vaira Ranch- Ione. FluxNet, University of California, Berkeley, https://www.osti.gov/servlets/purl/1440094.

Belelli, L., D. Papale, and R. Valentini, 2016: FLUXNET2015 RU-Ha1 Hakasia Steppe. FluxNet, University of Tuscia - Viterbo, https://www.osti.gov/servlets/purl/1440184.

Bell, B., and Coauthors, 2021: The ERA5 global reanalysis: Preliminary extension to 1950. Quart. J. Roy. Meteor. Soc., 147, 4186–4227, https://doi.org/10.1002/qj.4174.

Berbigier, P., J. Bonnefond, A. Bosc, P. Trichet, and D. Loustau, 2016: FLUXNET2015 Fr-Lbr Le Bray. FluxNet, INRA - UMR ISPA, https://www.osti.gov/servlets/purl/1440163.

Beringer, J., and L. Hutley, 2016a: FLUXNET2015 AU-Ade Adelaide River. FluxNet, Monash University, Charles Darwin University, https://www.osti.gov/servlets/purl/1440193.

——, and ——, 2016b: FLUXNET2015 AU-DaP Daly River Savanna. FluxNet, Monash University, Charles Darwin University, https://www.osti.gov/servlets/purl/1440123.

——, and ——, 2016c: FLUXNET2015 Au-Dry Dry River. FluxNet, Monash University, University of Western Australia, Charles Darwin University, https://www.osti.gov/servlets/purl/1440197.

——, and ——, 2016d: FLUXNET2015 AU-Fog Fogg Dam. FluxNet, Monash University, Charles Darwin University, https://www.osti.gov/servlets/purl/1440124.

——, and ——, 2016e: FLUXNET2015 AU-How Howard Springs. FluxNet, Charles Darwin University, University of Western Australia, Monash University, https://www.osti.gov/servlets/purl/1440125.

——, and ——, 2016f: FLUXNET2015 AU-Stp Sturt Plains. FluxNet, University of Western Australia, Charles Darwin University, Monash University, https://www.osti.gov/servlets/purl/1440204.

——, and ——, 2016g: FLUXNET2015 AU-DaS daly river cleared. FluxNet, University of Western Australia, https://www.osti.gov/servlets/purl/1440122.

——, and J. Walker, 2016: FLUXNET2015 Au-Ync Jaxa. FluxNet, University of Western Australia, Monash University, https://www.osti.gov/servlets/purl/1440208.

——, S. Cunningham, P. Baker, T. Cavagnaro, R. MacNally, R. Thompson, and I. McHugh, 2016a: FLUXNET2015 AU-Rig Riggs Creek. FluxNet, Monash University, https://www.osti.gov/servlets/purl/1440202.

——, ——, ——, ——, ——, ——, and ——, 2016b: FLUXNET2015 AU-Whr Whroo. FluxNet, Monash University, https://www.osti.gov/servlets/purl/1440206.

——, L. Hutley, D. McGuire, U. Paw, and I. McHugh, 2016c: FLUXNET2015 AU-WaC Wallaby Creek. FluxNet, Monash University, https://www.osti.gov/servlets/purl/1440127.

Bernhofer, C., T. Grünwald, U. Moderow, M. Hehn, U. Eichelmann, H. Prasse, and U. Postel, 2016a: FLUXNET2015 DE-Gri Grillenburg. FluxNet, TU Dresden, https://www.osti.gov/servlets/purl/1440147.

——, ——, ——, ——, ——, ——, and ——, 2016b: FLUXNET2015 DE-Kli Klingenberg. FluxNet, TU Dresden, https://www.osti.gov/servlets/purl/1440149.

——, ——, ——, ——, ——, ——, and ——, 2016c: FLUXNET2015 DE-Obe Oberbärenburg. FluxNet, TU Dresden, https://www.osti.gov/servlets/purl/1440151.

——, ——, ——, ——, ——, ——, and ——, 2016d: FLUXNET2015 DE-Spw Spreewald. FluxNet, TU Dresden, https://www.osti.gov/servlets/purl/1440220.

——, ——, ——, ——, ——, ——, and ——, 2016e: FLUXNET2015 DE-Tha Tharandt. FluxNet, TU Dresden, https://www.osti.gov/servlets/purl/1440152.

Berveiller, D., N. Delpierre, E. Dufrêne, J.-Y. Pontailler, L. Vanbostal, B. Janvier, L. Mottet, and K. Cristinacce, 2016: FLUXNET2015 FR-Fon Fontainebleau-Barbeau. FluxNet, CNRS, https://www.osti.gov/servlets/purl/1440161.

Best, M. J., A. Beljaars, J. Polcher, and P. Viterbo, 2004: A proposed structure for coupling tiled surfaces with the planetary boundary layer. J. Hydrometeor., 5, 1271–1278, https://doi.org/10.1175/JHM-382.1.

Betts, A. K., and J. Ball, 1995: The FIFE surface diurnal cycle climate. J. Geophys. Res., 100, 25 679–25 693, https://doi.org/10.1029/94JD03121.

Billesbach, D., J. Bradford, and M. Torn, 2016a: FLUXNET2015 US-AR1 ARM USDA UNL OSU Woodward Switchgrass 1. FluxNet, Lawerence Berkeley National Lab, U.S. Department of Agriculture, University of Nebraska, https://www.osti.gov/servlets/purl/1440103.

——, ——, and ——, 2016b: FLUXNET2015 US-AR2 ARM USDA UNL OSU Woodward Switchgrass 2. FluxNet, Lawrence Berkeley National Lab, U.S. Department of Agriculture, University of Nebraska, https://www.osti.gov/servlets/purl/1440104.

Biraud, S., M. Fischer, S. Chan, and M. Torn, 2016: FLUXNET2015 US-ARM ARM Southern Great Plains site - Lamont. FluxNet, Lawrence Berkeley National Laboratory, https://www.osti.gov/servlets/purl/1440066.

Black, T. A., 2016a: FLUXNET2015 CA-OAS Saskatchewan - Western Boreal, mature aspen. FluxNet, The University of British Columbia, https://www.osti.gov/servlets/purl/1440043.

——, 2016b: FLUXNET2015 CA-OBS Saskatchewan - Western Boreal, mature black spruce. FluxNet, The University of British Columbia, https://www.osti.gov/servlets/purl/1440044.

Blanken, P. D., R. K. Monson, S. P. Burns, D. R. Bowling, and A. A. Turnipseed, 2016: FLUXNET2015 US-NR1 Niwot Ridge forest (LTER NWT1). FluxNet, University of Colorado, https://www.osti.gov/servlets/purl/1440087.

Bonal, D., and B. Burban, 2016: FLUXNET2015 GF-Guy Guyaflux (French Guiana). FluxNet, https://www.osti.gov/servlets/purl/1440165.

Bourque, C.-A., and P. Arp, 1994: Dawn-to-dusk evolution of air turbulence, temperature and sensible and latent heat fluxes above a forest canopy: Concepts, model and field comparisons. Atmos.–Ocean, 32, 299–334, https://doi.org/10.1080/07055900.1994.9649500.

Bowling, D., 2016: FLUXNET2015 US-Cop Corral Pocket. FluxNet, University of Utah, https://www.osti.gov/servlets/purl/1440100.

Braganza, K., D. J. Karoly, and J. M. Arblaster, 2004: Diurnal temperature range as an index of global climate change during the twentieth century. Geophys. Res. Lett., 31, L13217, https://doi.org/10.1029/2004GL019998.

Bright, R. M., E. Davin, T. O'Halloran, J. Pongratz, K. Zhao, and A. Cescatti, 2017: Local temperature response to land cover and management change driven by non-radiative processes. Nat. Climate Change, 7, 296–302, https://doi.org/10.1038/nclimate3250.

Brovkin, V., and Coauthors, 2006: Biogeophysical effects of historical land cover changes simulated by six Earth system models of intermediate complexity. Climate Dyn., 26, 587–600, https://doi.org/10.1007/s00382-005-0092-6.

Brümmer, C., A. M. Lucas-Moffat, M. Herbst, O. Kolle, and J.-P. Delorme 2016: FLUXNET2015 DE-GEB Gebesee. FluxNet, Thünen Institute of Climate-Smart Agriculture, Braunschweig, https://www.osti.gov/servlets/purl/1440146.

Brutsaert, W., 2013: Evaporation into the Atmosphere: Theory, History and Applications, Vol. 1. Springer, 409 pp.

Buysse, P., B. Durand, J.-C. Gueudet, N. Mascher, E. Larmanou, P. Cellier, and B. Loubet, 2016: FLUXNET2015 FR-Gri Grignon. FluxNet, French National Institute for Agricultural Research, https://www.osti.gov/servlets/purl/1440162.

Cañete, E., P. Ortiz, M. Jimenez, F. Poveda, O. Priego, A. Ballesteros, and A. Kowalski, 2016: FLUXNET2015 ES-LJu Llano De Los Juanes. FluxNet, University of Granada, https://www.osti.gov/servlets/purl/1440157.

Cescatti, A., B. Marcolla, R. Zorer, and D. Gianelle, 2016: FLUXNET2015 IT-La2 Lavarone2. FluxNet, Centro di Ecologia Alpina, https://www.osti.gov/servlets/purl/1440235.

Chen, J., 2016a: FLUXNET2015 US-Wi3 Mature Hardwood (MHW). FluxNet, Michigan State University, https://www.osti.gov/servlets/purl/1440057.

——, 2016b: FLUXNET2015 US-Wi4 Mature Red Pine (MRP). FluxNet, Michigan State University, https://www.osti.gov/servlets/purl/1440058.

——, 2016c: FLUXNET2015 US-Wi6 Pine Barrens. FluxNet, Michigan State University, https://www.osti.gov/servlets/purl/1440060.

——, 2016d: FLUXNET2015 US-Wi9 Young Jack Pine (YJP). FluxNet, Michigan State University, https://www.osti.gov/servlets/purl/1440063.

——, H. Chu, and A. Noormets, 2016: FLUXNET2015 UU-Oho Oak Openings. FluxNet, University of Toledo/Michigan State University, https://www.osti.gov/servlets/purl/1440088.

Chen, L., and P. A. Dirmeyer, 2019a: Differing responses of the diurnal cycle of land surface and air temperatures to deforestation. *J. Climate*, **32**, 7067–7079, https://doi.org/10.1175/JCLI-D-19-0002.1.

——, and ——, 2019b: The relative importance among anthropogenic forcings of land use/land cover change in affecting temperature extremes. *Climate Dyn.*, **52**, 2269–2285, https://doi.org/10.1007/s00382-018-4250-z.

Chen, S., 2016: FLUXNET2015 CN-Du2 Duolun grassland (d01). FluxNet, Institute of Botany, Chinese Academy of Sciences, https://www.osti.gov/servlets/purl/1440140.

Claussen, M., V. Brovkin, and A. Ganopolski, 2001: Biogeophysical versus biogeochemical feedbacks of large-scale land cover change. *Geophys. Res. Lett.*, **28**, 1011–1014, https://doi.org/10.1029/2000GL012471.

Cleverly, J., D. Eamus, and P. Isaac, 2016a: FLUXNET2015 AU-ASM Alice Springs. FluxNet, University of Technology Sydney, https://www.osti.gov/servlets/purl/1440194.

——, ——, and ——, 2016b: FLUXNET2015 AU-TTE Ti Tree East. FluxNet, University of Technology Sydney, https://www.osti.gov/servlets/purl/1440205.

Collatz, G. J., L. Bounoua, S. O. Los, D. A. Randall, I. Y. Fung, and P. J. Sellers, 2000: A mechanism for the influence of vegetation on the response of the diurnal temperature range to changing climate. *Geophys. Res. Lett.*, **27**, 3381–3384, https://doi.org/10.1029/1999GL010947.

Copernicus Climate Change Service, 2019: ERA5-land hourly data from 2001 to present. ECMWF, downloaded 1 November 2020, https://cds.climate.copernicus.eu/doi/10.24381/cds.e2161bac.

Cremonese, E., M. Galvagno, U. M. Di Cella, and M. Migliavacca, 2016: FLUXNET2015 IT-Tor Torgnon. FluxNet, Environmental Protection Agency of Aosta Valley, https://www.osti.gov/servlets/purl/1440237.

Dai, A., A. D. Del Genio, and I. Y. Fung, 1997: Clouds, precipitation and temperature range. *Nature*, **386**, 665–666, https://doi.org/10.1038/386665b0.

——, K. E. Trenberth, and T. R. Karl, 1999: Effects of clouds, soil moisture, precipitation, and water vapor on diurnal temperature range. *J. Climate*, **12**, 2451–2473, https://doi.org/10.1175/1520-0442(1999)012<2451:EOCSMP>2.0.CO;2.

——, T. R. Karl, B. Sun, and K. E. Trenberth, 2006: Recent trends in cloudiness over the United States: A tale of monitoring inadequacies. *Bull. Amer. Meteor. Soc.*, **87**, 597–606, https://doi.org/10.1175/BAMS-87-5-597.

Davin, E. L., and N. de Noblet-Ducoudré, 2010: Climatic impact of global-scale deforestation: Radiative versus nonradiative processes. *J. Climate*, **23**, 97–112, https://doi.org/10.1175/2009JCLI3102.1.

De Kauwe, M. G., B. E. Medlyn, J. Knauer, and C. A. Williams, 2017: Ideas and perspectives: How coupled is the vegetation to the boundary layer? *Biogeosciences*, **14**, 4435–4453, https://doi.org/10.5194/bg-14-4435-2017.

De Ligne, A., T. Manise, B. Heinesch, M. Aubinet, and C. Vincke, 2016a: FLUXNET2015 BE-Vie Vielsalm. FluxNet, University of Liege - Gembloux Agro-Bio Tech, University catholic of Louvain-la-Neuve, https://www.osti.gov/servlets/purl/1440130.

——, ——, C. Moureaux, M. Aubinet, and B. Heinesch, 2016b: FLUXNET2015 BE-Lon Lonzee. FluxNet, University of Liege - Gembloux Agro-Bio Tech, https://www.osti.gov/servlets/purl/1440129.

Denissen, J. M., R. Orth, H. Wouters, D. G. Miralles, C. C. van Heerwaarden, J. V.-G. de Arellano, and A. J. Teuling, 2021: Soil moisture signature in global weather balloon soundings. *npj Climate Atmos. Sci.*, **4**, 13, https://doi.org/10.1038/s41612-021-00167-w.

Desai, A., 2016a: FLUXNET2015 US-Los Lost Creek. FluxNet, University of Wisconsin, https://www.osti.gov/servlets/purl/1440076.

——, 2016b: FLUXNET2015 US-PFa Park Falls/Wlef. FluxNet, University of Wisconsin, https://www.osti.gov/servlets/purl/1440089.

——, 2016c: FLUXNET2015 US-Syv Sylvania Wilderness Area. FluxNet, University of Wisconsin, https://www.osti.gov/servlets/purl/1440091.

——, 2016d: FLUXNET2015 US-WCr Willow Creek. FluxNet, University of Wisconsin, https://www.osti.gov/servlets/purl/1440095.

Diak, G. R., 1990: Evaluation of heat flux, moisture flux and aerodynamic roughness at the land surface from knowledge of the pbl height and satellite-derived skin temperatures. *Agric. For. Meteor.*, **52**, 181–198, https://doi.org/10.1016/0168-1923(90)90105-F.

Dirmeyer, P. A., and K. L. Brubaker, 2007: Characterization of the global hydrologic cycle from a back-trajectory analysis of atmospheric water vapor. *J. Hydrometeor.*, **8**, 20–37, https://doi.org/10.1175/JHM557.1.

Dolman, H., D. Hendriks, F.-J. Parmentier, L. B. Marchesini, J. Dean, and K. Van Huissteden, 2016: FLUXNET2015 NL-Hor horstermeer. FluxNet, Vrije Universiteit Amsterdam, https://www.osti.gov/servlets/purl/1440177.

Drake, B., and R. Hinkle, 2016a: FLUXNET2015 US-KS1 Kennedy Space Center (Slash Pine). FluxNet, Smithsonian Environmental Research Center, University of Central Florida, https://www.osti.gov/servlets/purl/1440074.

——, and ——, 2016b: FLUXNET2015 US-KS2 Kennedy Space Center (Scrub Oak). FluxNet, Smithsonian Environmental Research Center, University of Central Florida, URL https://www.osti.gov/servlets/purl/1440075.

Dusek, J., D. Janous, and M. Pavelka, 2016: FLUXNET2015 Cz-Wet Trebon (Czechwet). FluxNet, Global Change Research Institute CAS, https://www.osti.gov/servlets/purl/1440145.

Easterling, D. R., and Coauthors, 1997: Maximum and minimum temperature trends for the globe. *Science*, **277**, 364–367, https://doi.org/10.1126/science.277.5324.364.

ECMWF, 2007: IFS documentation CY31R1 - Part IV: Physical processes. ECMWF, https://www.ecmwf.int/node/9221.

Ermida, S. L., I. F. Trigo, C. C. DaCamara, F. M. Gottsche, F. S. Olesen, and G. Hulley, 2014: Validation of remotely sensed surface temperature over an oak woodland landscape—The problem of viewing and illumination geometries. *Remote Sens. Environ.*, **148**, 16–27, https://doi.org/10.1016/j.rse.2014.03.016.

Ewers, B., and E. Pendall, 2016: FLUXNET2015 US-Sta Saratoga. FluxNet, University of Wyoming, https://www.osti.gov/servlets/purl/1440115.

Falge, E., and Coauthors, 2017a: FLUXNET research network site characteristics, investigators, and bibliography, 2016. ORNL DAAC, https://doi.org/10.3334/ORNLDAAC/1530.

——, and Coauthors, 2017b: FLUXNET research network site characteristics, investigators, and bibliography, 2016. ORNL Distributed Active Archive Center, https://daac.ornl.gov/cgi-bin.

Fares, S., F. Savi, and A. Conte, 2016: FLUXNET2015 IT-Cp2 Castelporziano 2. FluxNet, Council for Agricultural Research and Economics, https://www.osti.gov/servlets/purl/1440233.

Feddema, J. J., K. W. Oleson, G. B. Bonan, L. O. Mearns, L. E. Buja, G. A. Meehl, and W. M. Washington, 2005: The importance of land-cover change in simulating future climates. *Science*, **310**, 1674–1678, https://doi.org/10.1126/science.1118160.

Gallo, K. P., D. R. Easterling, and T. C. Peterson, 1996: The influence of land use/land cover on climatological values of the diurnal temperature range. *J. Climate*, **9**, 2941–2944, https://doi.org/10.1175/1520-0442(1996)009<2941:TIOLUC>2.0.CO;2.

Garcia, M., N. Fernández, L. Villagarcía, F. Domingo, J. Puigdefábregas, and I. Sandholt, 2014: Accuracy of the Temperature–Vegetation Dryness Index using MODIS under water-limited vs. energy-limited evapotranspiration conditions. *Remote Sens. Environ.*, **149**, 100–117, https://doi.org/10.1016/j.rse.2014.04.002.

Gentine, P., A. Massmann, B. R. Lintner, S. H. Alemohammad, R. Fu, J. K. Green, D. Kennedy, and J. V.-G. de Arellano, 2019: Land–atmosphere interactions in the tropics—A review. *Hydrol. Earth Syst. Sci.*, **23**, 4171–4197, https://doi.org/10.5194/hess-23-4171-2019.

Gianelle, D., M. Cavagna, R. Zampedri, and B. Marcolla, 2016a: FLUXNET2015 IT-MBo Monte Bondone. FluxNet, Edmund Mach Foundation, https://www.osti.gov/servlets/purl/1440170.

——, R. Zampedri, M. Cavagna, and M. Sottocornola, 2016b: FLUXNET2015 IT-Lav Lavarone. FluxNet, Edmund Mach Foundation, https://www.osti.gov/servlets/purl/1440169.

Goldstein, A., 2016: FLUXNET2015 US-Blo Blodgett Forest. FluxNet, University of California, Berkeley, https://www.osti.gov/servlets/purl/1440068.

Gough, C., G. Bohrer, and P. Curtis, 2016a: FLUXNET2015 US-UMB Univ. of Mich. Biological Station. FluxNet, Ohio State University, Virginia Commonwealth University, https://www.osti.gov/servlets/purl/1440093.

——, ——, and ——, 2016b: FLUXNET2015 US-UMd UMBS disturbance. FluxNet, Ohio State University, Virginia Commonwealth University, https://www.osti.gov/servlets/purl/1440101.

Goulden, M., 2016a: FLUXNET2015 BR-Sa3 Santarem-Km83-logged forest. FluxNet, University of California, Irvine, https://www.osti.gov/servlets/purl/1440033.

——, 2016b: FLUXNET2015 CA-Ns1 UCI-1850 burn site. FluxNet, University of California, Irvine, https://www.osti.gov/servlets/purl/1440036.

——, 2016c: FLUXNET2015 CA-Ns2 UCI-1930 burn site. FluxNet, University of California, Irvine, https://www.osti.gov/servlets/purl/1440037.

——, 2016d: FLUXNET2015 CA-Ns3 UCI-1964 burn site. FluxNet, University of California, Irvine, https://www.osti.gov/servlets/purl/1440038.

——, 2016e: FLUXNET2015 CA-Ns4 UCI-1964 burn site wet. FluxNet, University of California, Irvine, https://www.osti.gov/servlets/purl/1440039.

——, 2016f: FLUXNET2015 CA-Ns5 UCI-1981 burn site. FluxNet, University of California, Irvine, https://www.osti.gov/servlets/purl/1440040.

——, 2016g: FLUXNET2015 CA-Ns6 UCI-1989 burn site. FluxNet, University of California, Irvine, https://www.osti.gov/servlets/purl/1440041.

——, 2016h: FLUXNET2015 CA-Ns7 UCI-1998 burn site. FluxNet, University of California, Irvine, https://www.osti.gov/servlets/purl/1440042.

Green, J. K., A. G. Konings, S. H. Alemohammad, J. Berry, D. Entekhabi, J. Kolassa, J.-E. Lee, and P. Gentine, 2017: Regionally strong feedbacks between the atmosphere and terrestrial biosphere. *Nat. Geosci.*, **10**, 410–414, https://doi.org/10.1038/ngeo2957.

Gruening, C., I. Goded, A. Cescatti, and O. Pokorska, 2016a: FLUXNET2015 IT-Isp Ispra ABC-IS. FluxNet, European Commission, Joint Research Centre, https://www.osti.gov/servlets/purl/1440234.

——, ——, ——, and ——, 2016b: FLUXNET2015 IT-SR2 San Rossore 2. FluxNet, European Commission, Joint Research Centre, https://www.osti.gov/servlets/purl/1440236.

Gu, L., and Coauthors, 2007: Influences of biomass heat and biochemical energy storages on the land surface fluxes and radiative temperature. *J. Geophys. Res.*, **112**, D02107, https://doi.org/10.1029/2006JD007425.

Helbig, M., and Coauthors, 2020: Whitepaper: Understanding land–atmosphere interactions through tower-based flux and continuous atmospheric boundary layer measurements. Ameriflux, 45 pp., http://ameriflux.lbl.gov/community/highlight/whitepaper-understanding-land-atmosphere-interactions-through-tower-based-flux-and-continuous-atmospheric-boundary-layer-measurements/.

Hörtnagl, L., W. Eugster, N. Buchmann, E. Paul-Limoges, S. Etzold, M. Haeni, and P. Pluess, and T. Baur, 2016a: FLUXNET2015 CH-Lae Laegern. FluxNet, ETH Zurich, https://www.osti.gov/servlets/purl/1440134.

——, and Coauthors, 2016b: FLUXNET2015 CH-Dav Davos. FluxNet, ETH Zurich, https://www.osti.gov/servlets/purl/1440132.

——, and Coauthors, 2016c: FLUXNET2015 CH-Fru Früebüel. FluxNet, ETH Zurich, https://www.osti.gov/servlets/purl/1440133.

——, and Coauthors, 2016d: FLUXNET2015 CH-Oe2 Oensingen Crop. FluxNet, ETH Zurich, https://www.osti.gov/servlets/purl/1440136.

Humes, K. S., W. P. Kustas, M. S. Moran, W. D. Nichols, and M. A. Weltz, 1994: Variability of emissivity and surface temperature over a sparsely vegetated surface. *Water Resour. Res.*, **30**, 1299–1310, https://doi.org/10.1029/93WR03065.

Ibrom, A., and K. Pilegaard, 2016: FLUXNET2015 DK-Sor Soroe. FluxNet, Technical University of Denmark (DTU), https://www.osti.gov/servlets/purl/1440155.

Jarvis, P. G., 1985: Transpiration and assimilation of tree and agricultural crops: The omega factor. *Attributes of Trees as Crop Plants*, M. G. R. Cannell and J. E. Jackson, Eds., Institute of Terrestrial Ecology, 460–480.

——, and K. G. McNaughton, 1986: Stomatal control of transpiration: Scaling up from leaf to region. *Adv. Ecol. Res.*, **15**, 1–49, https://doi.org/10.1016/S0065-2504(08)60119-1.

Jiang, H., Y. Yang, Y. Bai, and H. Wang, 2020: Evaluation of the total, direct, and diffuse solar radiations from the ERA5 reanalysis data in China. *IEEE Geosci. Remote Sens. Lett.*, **17**, 47–51, https://doi.org/10.1109/LGRS.2019.2916410.

Jin, M., and R. E. Dickinson, 2010: Land surface skin temperature climatology: Benefitting from the strengths of satellite observations. *Environ. Res. Lett.*, **5**, 044004, https://doi.org/10.1088/1748-9326/5/4/044004.

Johannsen, F., S. Ermida, J. P. A. Martins, I. F. Trigo, M. Nogueira, and E. Dutra, 2019: Cold bias of ERA5 summertime daily maximum land surface temperature over Iberian Peninsula. *Remote Sens.*, **11**, 2570, https://doi.org/10.3390/rs11212570.

Kalma, J. D., T. R. McVicar, and M. F. McCabe, 2008: Estimating land surface evaporation: A review of methods using remotely sensed surface temperature data. *Surv. Geophys.*, **29**, 421–469, https://doi.org/10.1007/s10712-008-9037-z.

Karl, T. R., G. Kukla, V. N. Razuvayev, M. J. Changery, R. G. Quayle, R. R. Heim, Jr., D. R. Easterling, and C. B. Fu, 1991: Global warming: Evidence for asymmetric diurnal temperature change. *Geophys. Res. Lett.*, **18**, 2253–2256, https://doi.org/10.1029/91GL02900.

Klatt, J., H. P. Schmid, M. Mauder, and R. Steinbrecher, 2016: FLUXNET2015 DE-Sfn Schechenfilz Nord. FluxNet, Karlsruhe Institute of Technology, IMK-IFU, https://www.osti.gov/servlets/purl/1440219/.

Kleidon, A., and M. Heimann, 2000: Assessing the role of deep rooted vegetation in the climate system with model simulations: Mechanism, comparison to observations and implications for Amazonian deforestation. *Climate Dyn.*, **16**, 183–199, https://doi.org/10.1007/s003820050012.

——, and M. Renner, 2017: An explanation for the different climate sensitivities of land and ocean surfaces based on the diurnal cycle. *Earth Syst. Dyn.*, **8**, 849–864, https://doi.org/10.5194/esd-8-849-2017.

——, and ——, 2018: Diurnal land surface energy balance partitioning estimated from the thermodynamic limit of a cold heat engine. *Earth Syst. Dyn.*, **9**, 1127–1140, https://doi.org/10.5194/esd-9-1127-2018.

Knohl, A., F. Tiedemann, O. Kolle, E.-D. Schulze, P. Anthoni, W. Kutsch, M. Herbst, and L. Siebicke, 2016a: FLUXNET2015 DE-Lnf Leinefelde. FluxNet, University of Goettingen, Bioclimatology, https://www.osti.gov/servlets/purl/1440150/.

——, ——, ——, ——, W. Kutsch, M. Herbst, and L. Siebicke, 2016b: FLUXNET2015 DE-Hai Hainich. FluxNet, University of Goettingen, Bioclimatology, https://www.osti.gov/servlets/purl/1440148.

Koster, R., and Coauthors, 2011: The second phase of the Global Land-Atmosphere Coupling Experiment: Soil moisture contributions to subseasonal forecast skill. *J. Hydrometeor.*, **12**, 805–822, https://doi.org/10.1175/2011JHM1365.1.

Kosugi, Y., and S. Takanashi, 2016: FLUXNET2015 MY-PSO Pasoh Forest Reserve (PSO). FluxNet, FRIM (Forest Research Institute of Malaysia), Kyoto University, https://www.osti.gov/servlets/purl/1440240.

Kotani, A., 2016a: FLUXNET2015 JP-MBF Moshiri Birch Forest Site. FluxNet, Nagoya University, https://www.osti.gov/servlets/purl/1440238.

——, 2016b: FLUXNET2015 JP-SMF Seto Mixed Forest Site. FluxNet, Nagoya University, https://www.osti.gov/servlets/purl/1440239.

Kumagai, T., T. M. Saitoh, Y. Sato, T. Morooka, O. J. Manfroi, K. Kuraji, and M. Suzuki, 2004: Transpiration, canopy conductance and the decoupling coefficient of a lowland mixed dipterocarp forest in Sarawak, Borneo: Dry spell effects. *J. Hydrol.*, **287**, 237–251, https://doi.org/10.1016/j.jhydrol.2003.10.002.

Kurc, S., 2016: FLUXNET2015 US-SRC Santa Rita Creosote. FluxNet, University of Arizona, https://www.osti.gov/servlets/purl/1440098

Kustas, W. P., and J. M. Norman, 1999: Evaluation of soil and vegetation heat flux predictions using a simple two-source model with radiometric temperatures for partial canopy cover. *Agric. For. Meteor.*, **94**, 13–29, https://doi.org/10.1016/S0168-1923(99)00005-2.

Kutsch, W. L., L. Merbold, and O. Kolle, 2016: FLUXNET2015 ZM-Mon Mongu. FluxNet, Max-Planck Institute for Biogeochemistry, https://www.osti.gov/servlets/purl/1440189.

Lauritsen, R. G., and J. C. Rogers, 2012: U.S. diurnal temperature range variability and regional causal mechanisms, 1901–2002. *J. Climate*, **25**, 7216–7231, https://doi.org/10.1175/JCLI-D-11-00429.1.

Law, B., 2016a: FLUXNET2015 US-Me1 Metolius - Eyerly Burn. FluxNet, Oregon State University, https://www.osti.gov/servlets/purl/1440078.

——, 2016b: FLUXNET2015 US-Me2 Metolius Mature Ponderosa Pine. FluxNet, Oregon State University, https://www.osti.gov/servlets/purl/1440079.

——, 2016c: FLUXNET2015 US-Me3 Metolius-Second Young Aged Pine. FluxNet, Oregon State University, https://www.osti.gov/servlets/purl/1440080.

——, 2016d: FLUXNET2015 US-Me4 Metolius-Old Aged Ponderosa Pine. FluxNet, Oregon State University, https://www.osti.gov/servlets/purl/1440081.

——, 2016e: FLUXNET2015 US-Me5 Metolius-First Young Aged Pine. FluxNet, Oregon State University, https://www.osti.gov/servlets/purl/1440082.

——, 2016f: FLUXNET2015 US-Me6 Metolius Young Pine Burn. FluxNet, Oregon State University, https://www.osti.gov/servlets/purl/1440099.

Lawrence, P. J., and Coauthors, 2012: Simulating the biogeochemical and biogeophysical impacts of transient land cover change and wood harvest in the Community Climate System Model (CCSM4) from 1850 to 2100. *J. Climate*, **25**, 3071–3095, https://doi.org/10.1175/JCLI-D-11-00256.1.

Lee, X., and T. A. Black, 1993: Atmospheric turbulence within and above a douglas-fir stand. Part II: Eddy fluxes of sensible heat and water vapour. *Bound.-Layer Meteor.*, **64**, 369–389, https://doi.org/10.1007/BF00711706.

Lewis, S. C., and D. J. Karoly, 2013: Evaluation of historical diurnal temperature range trends in CMIP5 models. *J. Climate*, **26**, 9077–9089, https://doi.org/10.1175/JCLI-D-13-00032.1.

Li, X., H. Chen, J. Wei, W. Hua, S. Sun, H. Ma, X. Li, and J. Li, 2018: Inconsistent responses of hot extremes to historical land use and cover change among the selected CMIP5 models. *J. Geophys. Res. Atmos.*, **123**, 3497–3512, https://doi.org/10.1002/2017JD028161.

Li, Y., 2016: FLUXNET2015 CN-Ha2 Haibei Shrubland. FluxNet, NWIPB Chinese Academy of Sciences, https://www.osti.gov/servlets/purl/1440211.

——, M. Zhao, S. Motesharrei, Q. Mu, E. Kalnay, and S. Li, 2015: Local cooling and warming effects of forests based on satellite observations. *Nat. Commun.*, **6**, 6603, https://doi.org/10.1038/ncomms7603.

Lin, Y.-S., and Coauthors, 2015: Optimal stomatal behaviour around the world. *Nat. Climate Change*, **5**, 459–464, https://doi.org/10.1038/nclimate2550.

Lindauer, M., R. Steinbrecher, B. Wolpert, M. Mauder, and H. P. Schmid, 2016: FLUXNET2015 DE-Lkb Lackenberg. FluxNet, Karlsruhe Institute of Technology, IMK-IFU, https://www.osti.gov/servlets/purl/1440214.

Lindroth, A., M. Mölder, and F. Lagergren, 2010: Heat storage in forest biomass improves energy balance closure. *Biogeosciences*, **7**, 301–313, https://doi.org/10.5194/bg-7-301-2010.

Lobell, D. B., and C. Bonfils, 2008: The effect of irrigation on regional temperatures: A spatial and temporal analysis of trends in California, 1934–2002. *J. Climate*, **21**, 2063–2071, https://doi.org/10.1175/2007JCLI1755.1.

Longobardi, P., A. Montenegro, H. Beltrami, and M. Eby, 2016: Deforestation induced climate change: Effects of spatial scale. *PLOS ONE*, **11**, e0153357, https://doi.org/10.1371/journal.pone.0153357.

MacFarlane, C., P. Lambert, J. Byrne, C. Johnstone, and N. Smart, 2016: FLUXNET2015 AU-Gin Gingin. FluxNet, Edith Cowan University (Centre for Ecosystem Management), https://www.osti.gov/servlets/purl/1440199.

Magliulo, V., and Coauthor, 2016: FLUXNET2015 IT-BCI BORGO CIOFFI. FluxNet, CNR ISAFOM, https://www.osti.gov/servlets/purl/1440166.

Mahmood, R., and Coauthors, 2014: Land cover changes and their biogeophysical effects on climate. *Int. J. Climatol.*, **34**, 929–953, https://doi.org/10.1002/joc.3736.

Makowski, K., E. B. Jaeger, M. Chiacchio, M. Wild, T. Ewen, and A. Ohmura, 2009: On the relationship between diurnal temperature range and surface solar radiation in Europe. *J. Geophys. Res.*, **114**, D00D07, https://doi.org/10.1029/2008JD011104.

Manca, G., and I. Goded, 2016: FLUXNET2015 IT-PT1 Parco Ticino forest. FluxNet, European Commission - DG Joint Research Centre, https://www.osti.gov/servlets/purl/1440172.

Margolis, H. A., 2016: FLUXNET2015 CA-QFO Quebec - Eastern boreal, mature black spruce. FluxNet, Universite Laval, https://www.osti.gov/servlets/purl/1440045.

Martens, B., D. L. Schumacher, H. Wouters, J. Muñoz-Sabater, N. E. C. Verhoest, and D. G. Miralles, 2020: Evaluating the land-surface energy partitioning in ERA5. *Geosci. Model Dev.*, **13**, 4159–4181, https://doi.org/10.5194/gmd-13-4159-2020.

Massman, B., 2016a: FLUXNET2015 US-GBT Glees Brooklyn tower. FluxNet, USDA Forest Service, https://www.osti.gov/servlets/purl/1440118.

——, 2016b: FLUXNET2015 US-GLE Glees. FluxNet, USDA Forest Service, https://www.osti.gov/servlets/purl/1440069.

Matamala, R., 2016: FLUXNET2015 US-IB2 Fermi National Accelerator Laboratory- Batavia (Prairie site). FluxNet, Argonne National Laboratory, https://www.osti.gov/servlets/purl/1440072.

Matteucci, G., 2016: FLUXNET2015 IT-COL Collelongo. FluxNet, Istituto di Ecologia e Idrologia Forestale CNR, https://www.osti.gov/servlets/purl/1440167.

McCaughey, H., 2016: FLUXNET2015 CA-GRO Ontario - Groundhog River, boreal mixedwood forest. FluxNet, Queen's University, https://www.osti.gov/servlets/purl/1440034.

Mearns, L. O., F. Giorgi, L. McDaniel, and C. Shields, 1995: Analysis of variability and diurnal range of daily temperature in a nested regional climate model: Comparison with observations and doubled CO_2 results. *Climate Dyn.*, **11**, 193–209, https://doi.org/10.1007/BF00215007.

Meier, R., E. L. Davin, S. C. Swenson, D. M. Lawrence, and J. Schwaab, 2019: Biomass heat storage dampens diurnal temperature variations in forests. *Environ. Res. Lett.*, **14**, 084026, https://doi.org/10.1088/1748-9326/ab2b4e.

Meinzer, F. C., G. Goldstein, N. M. Holbrook, P. Jackson, and J. Cavelier, 1993: Stomatal and environmental control of transpiration in a lowland tropical forest tree. *Plant Cell Environ.*, **16**, 429–436, https://doi.org/10.1111/j.1365-3040.1993.tb00889.x.

Merbold, L., K. Fuchs, N. Buchmann, and L. Hörtnagl, 2020: FLUXNET-CH4 CH-Cha Chamau. FluxNet, ETH Zurich, https://www.osti.gov/servlets/purl/1669629.

Meyer, W., P. Cale, G. Koerber, C. Ewenz, and Q. Sun, 2016: Fluxnet2015 AU-CPR Calperum. FluxNet;, University of Adelaide, https://www.osti.gov/servlets/purl/1440195/.

Meyers, T., 2016a: FLUXNET2015 US-GOO Goodwin creek. FluxNet, NOAA/ARL, https://www.osti.gov/servlets/purl/1440070/.

——, 2016b: FLUXNET2015 US-LWW little Washita watershed. FluxNet, NOAA/ARL, https://www.osti.gov/servlets/purl/1440077/.

Mildrexler, D. J., M. Zhao, and S. W. Running, 2011: A global comparison between station air temperatures and modis land surface temperatures reveals the cooling role of forests. *J. Geophys. Res.*, **116**, G03025, https://doi.org/10.1029/2010JG001486.

Miner, G. L., W. L. Bauerle, and D. D. Baldocchi, 2017: Estimating the sensitivity of stomatal conductance to photosynthesis: A review. *Plant Cell Environ.*, **40**, 1214–1238, https://doi.org/10.1111/pce.12871.

Montagnani, L., and S. Minerbi, 2016: FLUXNET2015 IT-REN renon. FluxNet, Autonomous Province of Bolzano, Forest Services, https://www.osti.gov/servlets/purl/1440173.

Moors, E., and J. Elbers, 2016: FLUXNET2015 NL-LOO Loobos. FluxNet, ALTERRA/Wageningen Environmental Research, https://www.osti.gov/servlets/purl/1440178.

Munger, J. W., 2016: FLUXNET2015 US-HA1 Harvard forest EMS tower (HFR1). FluxNet, Harvard University, https://www.osti.gov/servlets/purl/1440071.

Neirynck, J., H. Verbeeck, A. Carrara, A. S. Kowalski, R. Ceulemans, I. A. Janssens, B. Gielen, and M. Roland, 2016: FLUXNET2015 BE-Bra Brasschaat. FluxNet, University of Antwerp, https://doi.org/10.18140/FLX/1440128.

Nerry, F., J. Labed, and M.-P. Stoll, 1988: Emissivity signatures in the thermal IR band for remote sensing: Calibration procedure and method of measurement. *Appl. Opt.*, **27**, 758–764, https://doi.org/10.1364/AO.27.000758.

Norman, J. M., W. P. Kustas, and K. S. Humes, 1995: Source approach for estimating soil and vegetation energy fluxes in observations of directional radiometric surface temperature. *Agric. For. Meteor.*, **77**, 263–293, https://doi.org/10.1016/0168-1923(95)02265-Y.

Nouvellon, Y., 2016: FLUXNET2015 CG-Tch Tchizalamou. FluxNet, Centre de cooperation internationale en recherche agronomique pour le developpement, https://www.osti.gov/servlets/purl/1440142.

Novick, K., and R. Phillips, 2016: FLUXNET2015 US-MMS Morgan Monroe state forest. FluxNet, Indiana University, https://www.osti.gov/servlets/purl/1440083.

Nutini, F., M. Boschetti, G. Candiani, S. Bocchi, and P. Brivio, 2014: Evaporative fraction as an indicator of moisture condition and water stress status in semi-arid rangeland ecosystems. *Remote Sens.*, **6**, 6300–6323, https://doi.org/10.3390/rs6076300.

Olesen, J., 2016: FLUXNET2015 DK-Fou Foulum. FluxNet, Danish Institute of Agricultural Sciences, https://www.osti.gov/servlets/purl/1440154.

Ourcival, J.-M., K. Piquemal, R. Joffre, and L. Jean-Marc, 2016: FLUXNET2015 Fr-Pue puechabon. FluxNet, CNRS, https://www.osti.gov/servlets/purl/1440164.

Oyler, J. W., S. Z. Dobrowski, Z. A. Holden, and S. W. Running, 2016: Remotely sensed land skin temperature as a spatial predictor of air temperature across the conterminous United States. *J. Appl. Meteor. Climatol.*, **55**, 1441–1457, https://doi.org/10.1175/JAMC-D-15-0276.1.

Panwar, A., A. Kleidon, and M. Renner, 2019: Do surface and air temperatures contain similar imprints of evaporative

conditions? *Geophys. Res. Lett.*, **46**, 3802–3809, https://doi.org/10.1029/2019GL082248.

——, M. Renner, and A. Kleidon, 2020: Imprints of evaporative conditions and vegetation type in diurnal temperature variations. *Hydrol. Earth Syst. Sci.*, **24**, 4923–4942, https://doi.org/10.5194/hess-24-4923-2020.

Papale, D., and Coauthors, 2016: FLUXNET2015 IT-RO2 Roccarespampani 2. FluxNet, University of Tuscia - Viterbo, https://www.osti.gov/servlets/purl/1440175.

Pastorello, G., and Coauthors, 2020: The FLUXNET2015 dataset and the ONEFlux processing pipeline for eddy covariance data. *Sci. Data*, **7**, 225, https://doi.org/10.1038/s41597-020-0534-3.

Pendall, E., A. Griebel, D. Metzen, and C. Barton, 2016: FLUXNET2015 AU-Cum Cumberland Plains. FluxNet, Western Sydney University, https://www.osti.gov/servlets/purl/1440196.

Pilegaard, K., and A. Ibrom, 2016: FLUXNET2015 DK-Eng enghave. FluxNet, Technical University of Denmark (DTU), https://www.osti.gov/servlets/purl/1440153.

Pitman, A., and Coauthors, 2012: Effects of land cover change on temperature and rainfall extremes in multi-model ensemble simulations. *Earth Syst. Dyn.*, **3**, 213–231, https://doi.org/10.5194/esd-3-213-2012.

Poveda, F. D., A. L. Ballesteros, E. P. S. Cañete, P. S. Ortiz, M. R. M. Jiménez, O. P. Priego, and A. S. Kowalski, 2016: FLUXNET2015 ES-Amo Amoladeras. FluxNet, Estacion Experimental de Zona aridas (EEZA, CSIC), https://www.osti.gov/servlets/purl/1440156.

Pyrgou, A., M. Santamouris, and I. Livada, 2019: Spatiotemporal analysis of diurnal temperature range: Effect of urbanization, cloud cover, solar radiation, and precipitation. *Climate*, **7**, 89, https://doi.org/10.3390/cli7070089.

Reichstein, M., and Coauthors, 2005: On the separation of net ecosystem exchange into assimilation and ecosystem respiration: Review and improved algorithm. *Global Change Biol.*, **11**, 1424–1439, https://doi.org/10.1111/j.1365-2486.2005.001002.x.

Reverter, B. R., E. S. Perez-Canete, and A. S. Kowalski, 2016: FLUXNET2015 ES-LGS Laguna Seca. FluxNet, Universidad de Granada, https://www.osti.gov/servlets/purl/1440225.

Sabbatini, S., N. Arriga, B. Gioli, and D. Papale, M. Tomassucci, and A. Boschi, 2016a: FLUXNET2015 IT-CA2 Castel d'asso2. FluxNet, CNR IBIMET, University of Tuscia - Viterbo, https://www.osti.gov/servlets/purl/1440231.

——, ——, G. Matteucci, D. Papale, M. Tomassucci, and A. Boschi, 2016b: FLUXNET2015 IT-CA3 Castel d'asso 3. FluxNet, University of Tuscia - Viterbo, CNR IBAF, https://www.osti.gov/servlets/purl/1440232.

——, ——, D. Papale, M. Tomassucci, and A. Boschi, 2016c: FLUXNET2015 IT-CA1 Castel d'asso1. FluxNet, University of Tuscia - Viterbo, https://www.osti.gov/servlets/purl/1440230.

Sachs, T., C. Wille, E. Larmanou, and D. Franz, 2016: FLUXNET2015 DE-Zrk Zarnekow. FluxNet, GFZ German Research Centre for Geosciences, https://www.osti.gov/servlets/purl/1440221.

Saleska, S., 2016: FLUXNET2015 BR-SA1 Santarem-km67-primary forest. FluxNet, University of Arizona, https://www.osti.gov/servlets/purl/1440032.

Santanello, J. A., Jr., C. D. Peters-Lidard, and S. V. Kumar, 2011: Diagnosing the sensitivity of local land–atmosphere coupling via the soil moisture-boundary layer interaction. *J. Hydrometeor.*, **12**, 766–786, https://doi.org/10.1175/JHM-D-10-05014.1.

Schmidt, M., and A. Graf, 2016: FLUXNET2015 DE-RuR rollesbroich. FluxNet, IBG-3 Agrosphäre, Research Centre Jülich GmbH, https://www.osti.gov/servlets/purl/1440215.

Schneider, K., and M. Schmidt, 2016: FLUXNET2015 DE-SEH selhausen. FluxNet, University of Cologne, https://www.osti.gov/servlets/purl/1440217.

Scott, R., 2016a: FLUXNET2015 US-SRG Santa Rita Grassland. FluxNet, U.S. Department of Agriculture, https://www.osti.gov/servlets/purl/1440114.

——, 2016b: FLUXNET2015 US-SRM Santa Rita Mesquite. FluxNet, U.S. Department of Agriculture, https://www.osti.gov/servlets/purl/1440090.

——, 2016c: FLUXNET2015 US-Whs walnut gulch lucky hills shrub. FluxNet, U.S. Department of Agriculture, https://www.osti.gov/servlets/purl/1440097.

——, 2016d: FLUXNET2015 US-WKg Walnut Gulch Kendall grasslands. FluxNet, U.S. Department of Agriculture, https://www.osti.gov/servlets/purl/1440096.

Shi, P., X. Zhang, and Y. He, 2016: FLUXNET2015 Cn-Dan Dangxiong. FluxNet, IGSNRR Chinese Academy of Sciences, https://www.osti.gov/servlets/purl/1440138.

Sigut, L., K. Havrankova, G. Jocher, M. Pavelka, D. Janouš, K. Stanik, J. Trusina, and R. Czerny, 2016: FLUXNET2015 CZ-BK2 Bily Kriz grassland. FluxNet, Global Change Research Institute CAS, https://www.osti.gov/servlets/purl/1440144.

Simmons, A., and Coauthors, 2021: Low frequency variability and trends in surface air temperature and humidity from ERA5 and other datasets. Tech. Memo. 881, European Centre for Medium-Range Weather Forecasts, 99 pp., https://www.ecmwf.int/sites/default/files/elibrary/2021/19911-low-frequency-variability-and-trends-surface-air-temperature-and-humidity-era5-and-other.pdf.

Spano, D., and Coauthors, 2016: FLUXNET2015 IT-Noe arca di noe - le prigionette. FluxNet, University of Sassari, CNR-Ibimet Sassari, https://www.osti.gov/servlets/purl/1440171.

Stone, D. A., and A. J. Weaver, 2002: Daily maximum and minimum temperature trends in a climate model. *Geophys. Res. Lett.*, **29**, 1356, https://doi.org/10.1029/2001GL014556.

Stull, R. B., and Coauthors, 2015: *Practical Meteorology: An Algebra-Based Survey of Atmospheric Science.* University of British Columbia, 940 pp., https://www.eoas.ubc.ca/books/Practical_Meteorology/.

Sturtevant, C., D. Szutu, D. Baldocchi, J. H. Matthes, P. Oikawa, and S. D. Chamberlain, 2016: FLUXNET2015 US-MyB mayberry wetland. FluxNet, University of California, Berkeley, https://www.osti.gov/servlets/purl/1440105.

Su, Z., 2002: The Surface Energy Balance System (SEBS) for estimation of turbulent heat fluxes. *Hydrol. Earth Syst. Sci.*, **6**, 85–100, https://doi.org/10.5194/hess-6-85-2002.

Sun, Z., Q. Wang, O. Batkhishig, and Z. Ouyang, 2016: Relationship between evapotranspiration and land surface temperature under energy- and water-limited conditions in dry and cold climates. *Adv. Meteor.*, **2016**, 1835487, https://doi.org/10.1155/2016/1835487.

Suyker, A., 2016a: FLUXNET2015 US-Ne1 mead - irrigated continuous maize site. FluxNet, University of Nebraska, Lincoln, https://www.osti.gov/servlets/purl/1440084.

——, 2016b: FLUXNET2015 US-Ne2 mead - irrigated maize-soybean rotation site. FluxNet, University of Nebraska, Lincoln, https://www.osti.gov/servlets/purl/1440085.

——, 2016c: FLUXNET2015 US-Ne3 mead - rainfed maize-soybean rotation site. FluxNet, University of Nebraska, Lincoln, https://www.osti.gov/servlets/purl/1440086.

Swenson, S. C., S. P. Burns, and D. M. Lawrence, 2019: The impact of biomass heat storage on the canopy energy balance and atmospheric stability in the Community Land Model.

J. Adv. Model. Earth Syst., **11**, 83–98, https://doi.org/10.1029/2018MS001476.

Tagesson, T., J. Ardö, and R. Fensholt, 2016: FLUXNET2015 SN-Dhr Dahra. FluxNet, Lund University, https://www.osti.gov/servlets/purl/1440246.

Thome, K., 2014: ASTER global emissivity database: 100 times more detailed than its predecessors. NASA, https://terra.nasa.gov/news/aster-global-emissivity-database-100-times-more-detailed-than-its-predecessors.

Torn, M., 2016a: FLUXNET2015 US-ARb ARM Southern Great Plains burn site- lamont. FluxNet, Lawrence Berkeley National Laboratory, https://www.osti.gov/servlets/purl/1440064.

——, 2016b: FLUXNET2015 US-ARc ARM Southern Great Plains control site- lamont. FluxNet, Lawrence Berkeley National Laboratory, https://www.osti.gov/servlets/purl/1440065.

Trigo, I. F., L. F. Peres, C. C. DaCamara, and S. C. Freitas, 2008: Thermal land surface emissivity retrieved from SEVIRI/Meteosat. *IEEE Trans. Geosci. Remote Sens.*, **46**, 307–315, https://doi.org/10.1109/TGRS.2007.905197.

——, and Coauthors, 2011: The Satellite Application Facility for Land Surface Analysis. *Int. J. Remote Sens.*, **32**, 2725–2744, https://doi.org/10.1080/01431161003743199.

Urraca, R., T. Huld, A. Gracia-Amillo, F. J. Martinez-de Pison, F. Kaspar, and A. Sanz-Garcia, 2018: Evaluation of global horizontal irradiance estimates from ERA5 and COSMO-REA6 reanalyses using ground and satellite-based data. *Sol. Energy*, **164**, 339–354, https://doi.org/10.1016/j.solener.2018.02.059.

Valentini, R., S. Dore, F. Mazzenga, S. Sabbatini, P. Stefani, G. Tirone, and D. Papale, 2016a: FLUXNET2015 IT-Cpz Castelporziano. FluxNet, University of Tuscia - Viterbo, https://www.osti.gov/servlets/purl/1440168.

——, G. Nicolini, P. Stefani, A. De Grandcourt, and S. Stivanello, 2016b: FLUXNET2015 GH-Ank Ankasa. FluxNet, Euro Mediterranean Center for Climate Change - Viterbo, University of Tuscia - Viterbo, https://www.osti.gov/servlets/purl/1440229

——, and Coauthors, 2016c: FLUXNET2015 IT-Ro1 roccarespampani 1. FluxNet, University of Tuscia - Viterbo, https://www.osti.gov/servlets/purl/1440174.

Valor, E., and V. Caselles, 1996: Mapping land surface emissivity from NDVI: Application to European, African, and South American areas. *Remote Sens. Environ.*, **57**, 167–184, https://doi.org/10.1016/0034-4257(96)00039-9.

Varlagin, A., J. Kurbatova, and N. Vygodskaya, 2016: FLUXNET2015 RU-Fyo Fyodorovskoye. FluxNet, A.N. Severtsov Institute of Ecology and Evolution, https://www.osti.gov/servlets/purl/1440183.

Wang, H., and X. Fu, 2016: FLUXNET2015 CN-Qia Qianyanzhou. FluxNet, IGSNRR Chinese Academy of Sciences, https://www.osti.gov/servlets/purl/1440141.

Wang, K., and R. E. Dickinson, 2012: A review of global terrestrial evapotranspiration: Observation, modeling, climatology, and climatic variability. *Rev. Geophys.*, **50**, RG2005, https://doi.org/10.1029/2011RG000373.

Wang, X., and C. Prigent, 2020: Comparisons of diurnal variations of land surface temperatures from numerical weather prediction analyses, infrared satellite estimates and in situ measurements. *Remote Sens.*, **12**, 583, https://doi.org/10.3390/rs12030583.

Whitehead, D., P. G. Jarvis, and R. H. Waring, 1984: Stomatal conductance, transpiration, and resistance to water uptake in a *Pinus sylvestris* spacing experiment. *Can. J. For. Res.*, **14**, 692–700, https://doi.org/10.1139/x84-124.

Wohlfahrt, G., A. Hammerle, and L. Hörtnagl, 2016: FLUXNET2015 AT-NEU Neustift. FluxNet, University of Innsbruck, https://www.osti.gov/servlets/purl/1440121.

Wolf, S., W. Eugster, and N. Buchmann, 2016a: FLUXNET2015 Pa-Spn Sardinilla plantation. FluxNet, ETH Zurich, https://www.osti.gov/servlets/purl/1440180.

——, ——, and ——, 2016b: FLUXNET2015 Pa-Sps Sardinilla-Pasture. FluxNet, ETH Zurich, https://www.osti.gov/servlets/purl/1440179.

Woodgate, W., E. Van Gorsel, and R. Leuning, 2016: FLUXNET2015 AU-Tum Tumbarumba. FluxNet, CSIRO, https://www.osti.gov/servlets/purl/1440126.

Wouters, H., I. Y. Petrova, C. C. Heerwaarden, J. Vila-Guerau de Arellano, A. J. Teuling, V. Meulenberg, J. A. Santanello, and D. G. Miralles, 2019: Atmospheric boundary layer dynamics from balloon soundings worldwide: CLASS4GL v1.0. *Geosci. Model Dev.*, **12**, 2139–2153, https://doi.org/10.5194/gmd-12-2139-2019.

Zhang, J., and S. Han, 2016: FLUXNET2015 CN-Cha changbaishan. FluxNet, IAE Chinese Academy of Sciences, https://www.osti.gov/servlets/purl/1440137.

Zhang, W., Y. Huang, Y. Yu, and W. Sun, 2011: Empirical models for estimating daily maximum, minimum and mean air temperatures with MODIS land surface temperatures. *Int. J. Remote Sens.*, **32**, 9415–9440, https://doi.org/10.1080/01431161.2011.560622.

Zhou, G., and J. Yan, 2016: FLUXNET2015 CN-Din Dinghushan. FluxNet, SCIB Chinese Academy of Sciences, https://www.osti.gov/servlets/purl/1440139.

Zhou, L., R. E. Dickinson, Y. Tian, R. S. Vose, and Y. Dai, 2007: Impact of vegetation removal and soil aridation on diurnal temperature range in a semiarid region: Application to the Sahel. *Proc. Natl. Acad. Sci. USA*, **104**, 17 937–17 942, https://doi.org/10.1073/pnas.0700290104.

——, A. Dai, Y. Dai, R. S. Vose, C.-Z. Zou, Y. Tian, and H. Chen, 2009: Spatial dependence of diurnal temperature range trends on precipitation from 1950 to 2004. *Climate Dyn.*, **32**, 429–440, https://doi.org/10.1007/s00382-008-0387-5.